12-9-2006

Rans And Hybrid Rans/Les Computations For Three-Dimensional Wings With Ice Accretion

Mithun Varma Mankada Covilakom

RANS AND HYBRID RANS/LES COMPUTATIONS FOR THREE-DIMENSIONAL WINGS WITH ICE ACCRETION

By

Mithun Varma

A Thesis
Submitted to the Faculty of
Mississippi State University
in Partial Fulfillment of the Requirements
for the Degree of Master of Science
in Aerospace Engineering
in the Department of Aerospace Engineering

Mississippi State, Mississippi

December 2006

RANS AND HYBRID RANS/LES COMPUTATIONS FOR
THREE-DIMENSIONAL WINGS WITH
ICE ACCRETION

By

Mithun Varma

Approved:

Dr. David S. Thompson Associate Professor Aerospace Engineering (Major Professor)	Dr. Edward Luke Assistant Professor Computer Science and Engineering (Committee Member)
Dr. Keith Walters Assistant Professor Mechanical Engineering (Committee Member)	Dr. Pasquale Cinnella Professor of Aerospace Engineering (Graduate Coordinator)

Dr. Kirk H. Schulz
Dean of the Bagley
College of Engineering

Name: Mithun Varma

Date of Degree: December 8, 2006

Institution: Mississippi State University

Major Field: Engineering (Aerospace Engineering)

Major Professor: Dr. David S. Thompson

Title of Study: RANS AND HYBRID RANS/LES COMPUTATIONS FOR THREE-DIMENSIONAL WINGS WITH ICE ACCRETION

Pages in Study: 112

Candidate for Degree of Master of Science

Computational investigations were carried out to evaluate the e ectiveness and usability of hybrid RANS/LES techniques for predicting the unsteady separated flow over wings with ice accretion. RANS and hybrid RANS/LES computations were performed using the viscous flow solver CHEM with the SST turbulence model. Two configurations were considered during the study: an extruded wing with a glaze-ice shape and a swept wing with a simulated glaze-ice accretion. Hybrid RANS/LES results, in general, predict a less active shear layer "roll up" than seen in the experimental data. Qualitative improvements are seen in the hybrid RANS/LES results over corresponding RANS results. The extruded wing results show that the CHEM hybrid RANS/LES results are similar to the AVUS DES results. The use of preconditioning and a di erent turbulent model in CHEM showed a slight improvement in results.

DEDICATION

To Amma, for whom this means the most

ACKNOWLEDGMENTS

Long years ago, a psychologist, responding to a query at a session in my school, said - "God is gratitude". I am not sure If I may ever fathom exactly what he was trying to convey, but at least I have come to understand the importance of gratitude. And it is ever so important at this juncture. There are many people towards whom I am grateful to. Many who held my hand and led me through my studies here and during life in between. First and foremost, I would like to thank Dr. David S. Thompson for providing me the opportunity, the support, and the guidance (professional and personal) without which any of this would not have been possible. He patiently taught me a lot of things, and I am sure I will hold on to them. Thanks also for understanding me deeply. All in all, "Fatherly" is what comes to mind. I wish to thank my committee members who stood by me and helped me throughout: Dr. Edward Luke who stood my e-mail barrages and patiently answered all queries regarding the CHEM code and beyond, and Dr. Keith Walters for providing very valuable suggestions and insights.

I also o er my gratitude to my friends at the High Performance Computing Collaboratory (HPC^2) who guided me during this work: Dr. Ravi Balasubramaniam, Qingluan Xue, Dr. Shanti Bhushan, Dr. Satish Chalasani, are but a few. My heartfelt gratitude to my parents whose unconditional support and love I still take for granted. Thanks also for masking (rather poorly) your

worries and disguising them as yet another long-distance call. Special thanks to all my friends in Starkville, who made this place not just home away from home, but home itself.

This e ort was supported by NASA GRC (NNC05GA65G) with Dr. Mark Potapczuk as Technical Monitor. I wish to thank Trey Breckenridge, Roger L. Smith and Joey B. Jones of the HPC^2 system administration for their outstanding technical support on the HPC^2 clusters.

TABLE OF CONTENTS

CHAPTER Page

LIST OF TABLES

LIST OF FIGURES

FIGURE Page

FIGURE Page

FIGURE Page

NOMENCLATURE

$\mathcal{A}$	Cell face area
α	Angle of attack in degrees
c	Airfoil chord length
C_D	Drag coefficient
C_L	Lift coefficient
C_P	Pressure coefficient
Δ	Local mesh spacing
Δ_0	Mesh spacing in focus region
Δt_0	Estimated time step size to yield a local CFL number
e_0	Total energy of mixture
F_i	Inviscid flux vector
F_v	Viscous flux vector
h_s	Species enthalpy, $h_s = e_s + R_s T$
$\tilde{\tilde{I}}$	Identity tensor
k	Turbulent kinetic energy
M	Mach number
n	Time step
$\tilde{n}$	Unit vector normal to a surface
NS	Number of chemical species

Q	Vector of conservative variables
$\tilde{q}$	Heat conduction vector
R	Numerical residual
Re	Reynolds number based on the chord
t	Solution time
U_0	Maximum flow velocity in focus region
	of unity in the focus region
U_∞	Freestream velocity
$\tilde{u}$	Velocity vector
$\mathcal{V}$	Cell volume
$\tilde{V}_s$	Species mass di usion velocity
$\dot{W}$	Chemistry source term vector
$\dot{w}_s$	Species chemical production rate
y^+	Non-dimensional distance from the wall
λ	Wavelength of smallest resolved eddy
μ_t	Coefficient of turbulent viscosity
ν_t	Coefficient of eddy viscosity, $\nu_t = \mu_t/\rho$
ρ	Density of mixture
ρ_s	Species density
$\tilde{\tilde{\tau}}$	Stress tensor
	Magnitude of the vorticity vector
$_c$	Control volume of cell c
$\partial\ _c$	Boundary of cell c

CHAPTER I

INTRODUCTION

Ice accretion on aircraft is a source of concern in aviation. The hazards posed by in-flight as well as ground icing are varied in degree and e ect, but it is well accepted that they are never to be taken lightly. Ice accretion has been a contributing factor in a significant number of weather related aircraft accidents. From 1990 through 2000, 12% of all weather related accidents were attributed to icing [2].

Aircraft components such as the leading edges of wings, control surfaces, propellers, vents, intakes and cowlings face the brunt of in-flight aircraft icing. Ice accretion, especially on the wing leading edge, is a major concern for aircraft not equipped with anti-icing or de-icing mechanisms. The airframe must be at a sub-zero (celsius) temperature and should be flying through supercooled cloud or rain for ice accretion to occur with generally the worst continuous icing conditions being near the freezing level in heavily stratified clouds [8].

One focus of general icing research is on wing-airfoil icing and the resulting loss in lift and increase in drag. These e ects can vary significantly across di erent wing configurations. Airflow disruption, with complex unsteady separated flows behind the ice accretions, can significantly degrade the performance and handling characteristics of the aircraft. The presence of ice can reduce the maximum lift coefficient attainable by as much as 30% to 50% [9], thereby raising the stall speed

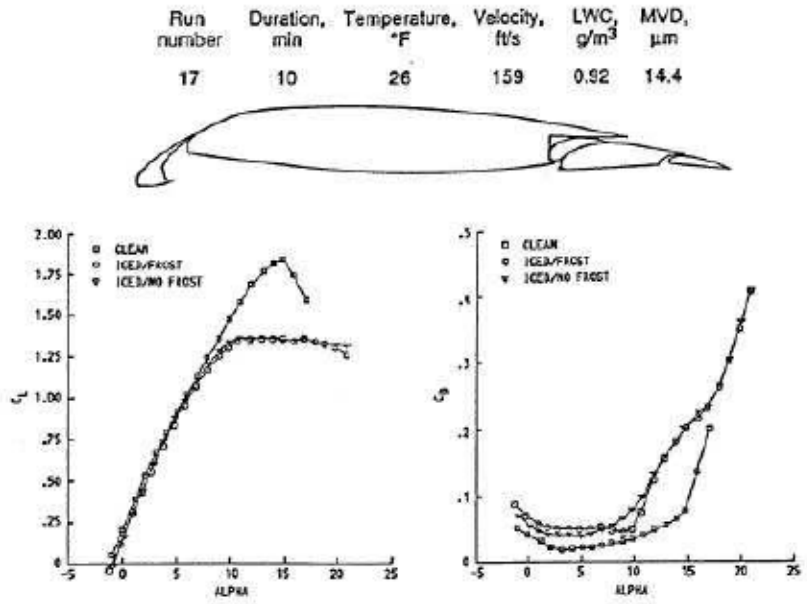

Figure 1.1: E ect of ice on lift and drag for the Boeing 737-200 wing model [1]

considerably. To maintain lift in icing conditions, the aircraft has to fly at a greater angle of attack thus increasing the induced drag by as much as 40% [9]. Other e ects of aircraft icing include changes in pitching moment that negatively impact control e ectiveness. Figure 1.1 shows the e ects of ice on lift and drag for the Boeing 737-200 wing model [1]. At higher angles of attack, significantly lower lift coefficients and larger drag coeffiecients are observed for the iced wing as compared to the clean wing configuration.

Ice accretions on straight wings are generally classified as rime, horn or spanwise-ridge, which are generally two dimensional in nature, and roughness, which is generally three dimensional [10]. This categorization is broad in nature, but in actuality, an ice accretion may also take shapes which have features borrowed from a combination of the above mentioned categories. In terms of aerodynamic

Figure 1.2: Wing leading edge horn ice [2]

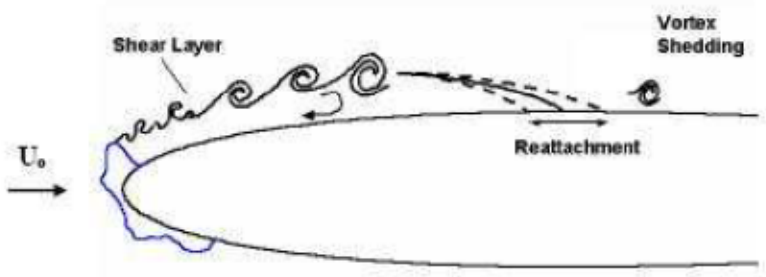

Figure 1.3: Schematic of upper surface separation bubble on an airfoil with a leading-edge horn ice accretion [3]

e ects, the spanwise-ridge ice shape generally exhibits greater e ects in comparison to e ects due to horn and rime ice [10]. Roughness occurs during the initial stages of the ice accretion process before a significant ice shape takes form and its e ects on the aerodynamics can be varied. The flow field over a wing with ice accretion may be unsteady and produce complex flow fields aft of the ice accretion.

Figure 1.2 shows leading-edge horn on an aircraft wing. The dominant flow feature associated with a horn ice-shape is the presence of a separation bubble just aft of the horn that has a major e ect on the global pressure distribution. Flow

separation occurs at the horn as the boundary layer cannot recover the pressure necessary to remain attached. The horn ice shape is of much interest because of the complex flow fields and unsteadiness it fosters and is the subject of this study. The schematic in figure 1.3 shows the complex flow associated with an airfoil with a horn ice accretion. The flow on the airfoil surface upstream of reattachment is reversed, whereas the flow aft of reattachment is streamwise. Figure 1.3 also depicts the variation of reattachment location with time and thereby the fluctuation of the reattachment zone due to the unsteady nature of the flow. Occasionally, vortices from the shear layer may be shed downstream.

Rime ice can be seen as special case of the horn with the horn oriented forward into the direction of the flow. The boundary layer remains attached on the upper surface of the horn. Flow separation may occur at the ice/airfoil intersection because of the existence of an adverse pressure gradient around that region. Spanwise-ridges are typically located farther downstream than the other types of ice accretions and, unlike the rime and horn ice shapes, the stagnation point is upstream of this ice shape.

1.1 Motivation

Although traditional Reynolds-Averaged Navier Stokes (RANS) simulations have contributed much to the prediction of flow properties around iced airfoils, they can not robustly capture the separation associated with iced airfoil flows as they employ turbulence models developed and validated for attached or free-shear layer flow conditions [11]. Large Eddy Simulation (LES) [12] methodology provides one alternative, but for high Reynolds number flows with massive flow separation, as seen in wings with ice accretion, the use of fully-resolved LES is prohibitively

expensive due to the small but dynamically important eddies present in the near-wall regions. Alternatives include the use of Detached Eddy Simulation (DES) [13] and other hybrid RANS/LES techniques [14, 15]. In such methodologies, a RANS model is used in the near-wall regions while LES is used away from the wall in the separated regions. Past research using hybrid RANS/LES techniques like DES for iced airfoils [16, 17, 18, 19] and other massively-separated flow problems have shown enough promise to pursue this technique.

Computational work done by Mogili [20] and Mogili *et al.* [21] on an extruded wing with GLC 305/944-ice shape with a rectangular planform using the Spalart-Allmaras DES technique provides the motivation for this current e ort. Mogili *et al.* [21], employed the AVUS code [22] to compute steady-state RANS solutions and DES solutions. These numerical results were evaluated by comparison with experimental data. Some mesh refinement studies were also undertaken.

While the RANS solutions significantly under-predicted the lift and drag coefficients, three-dimensional DES computations showed some improvement when compared to experimental data near stall at a 6° angle of attack. However, the length and position of the separation bubble formed aft of the ice-shape was overestimated. Comparisons between the predicted time-averaged midspan streamwise velocity and experimental data, as seen in figure 1.4, show that the separation region has been shifted aft of the experimental location. Although the predicted RMS of the fluctuations in the streamwise velocity agrees qualitatively with experimental data, the location of maximum intensity is shifted upward and to the right as shown in figure 1.5.

With the desire to better capture the unsteady flow field and to better predict the lift and drag coefficients, this e ort investigates alternate approaches. Following the recommendations and inferences drawn from the work of Mogili *et*

(a) DES solution as obtained by Mogili *et al.* [21]

(b) Experimental hot-split-film data [6]

Figure 1.4: Comparison of predicted three-dimensional time-averaged midspan streamwise velocity and experimental data for the extruded 944-glaze-ice shape at 6° angle of attack

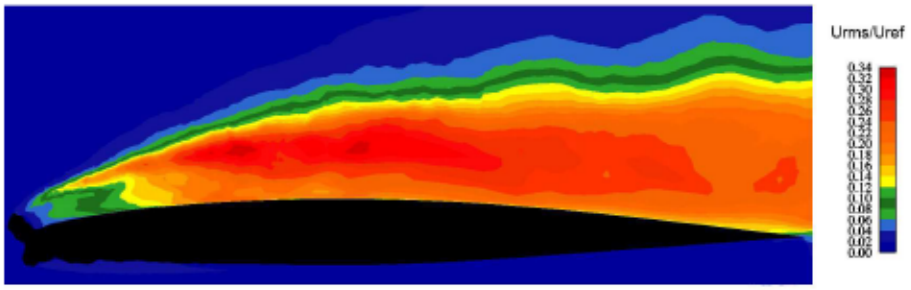

(a) DES results as obtained by Mogili *et al.* [21]

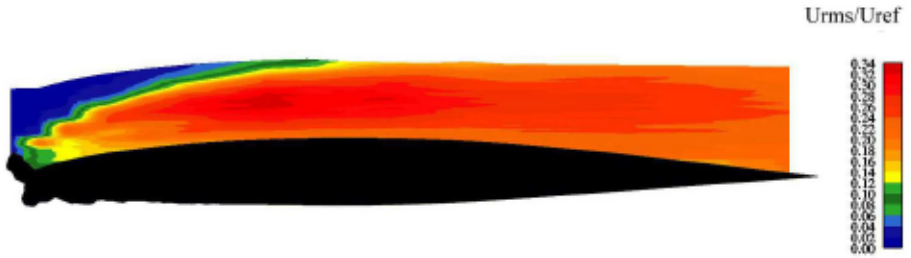

(b) Experimental hot-split-film data [6]

Figure 1.5: Comparison of RMS of the fluctuations in the streamwise velocity component for the extruded 944-glaze-ice shape at 6° angle of attack

al. [5], some approaches considered and the rationale for their consideration are given below:

- The use of preconditioning to modify the dissipation terms for the relatively low Mach number flow. The hypothesis is that the additional dissipation stabilizes the detached shear layer and delays roll up.

- The use of hybrid RANS/LES models other than the one-equation Spalart-Allmaras DES approach.

- The application of hybrid RANS/LES technique to a less severe ice-shape and wing geometry to assess whether a simpler geometry might yield better results.

With the above considerations in mind, the viscous flow solver CHEM [23, 24] was used to compute the flow field for the extruded wing problem. CHEM uses a finite-volume procedure to discretize the flow equations. Several turbulence models, including a family of two-equation models including the SST formulation by Menter [25], have been implemented in CHEM. CHEM was used to obtain RANS and hybrid RANS/LES solutions using the SST turbulence model for the extruded wing problem and comparisons were made with DES computations of Mogili [20] and with experimental data [5, 6]. Preconditioning was used in the flow solution. A swept wing configuration with a simpler, more benign ice accretion was also studied as part of this e ort. RANS and hybrid RANS/LES solutions were obtained using CHEM for the swept wing configuration and results were compared with experimental data [7].

Figure 1.6: Aircraft wing with GLC 305 airfoil section with two dimensional 944-glaze-ice shape (extruded wing)

1.2 Thesis statement

The overall objectives of the work reported in this thesis are to predict the aerodynamic e ects of ice accretions on wing configuration using available CFD methods and also to evaluate the e ectiveness of such methods. This e ort seeks to answer the question of whether the use of a di erent hybrid RANS/LES technique, the use of preconditioning, or the use of a di erent geometry produce better results in the treatment of separated flows due to ice accretions. The results obtained were evaluated by comparisons with available experimental data.

1.3 Overview of the present research

This e ort evaluates the e ectiveness and usability of hybrid RANS/LES techniques for predicting unsteady separated flow over wings with ice accretion. Hybrid RANS/LES simulations were carried out for two problems. One was an extruded wing case with a 944-glaze-ice shape on a GLC 305 airfoil [5, 6]. The

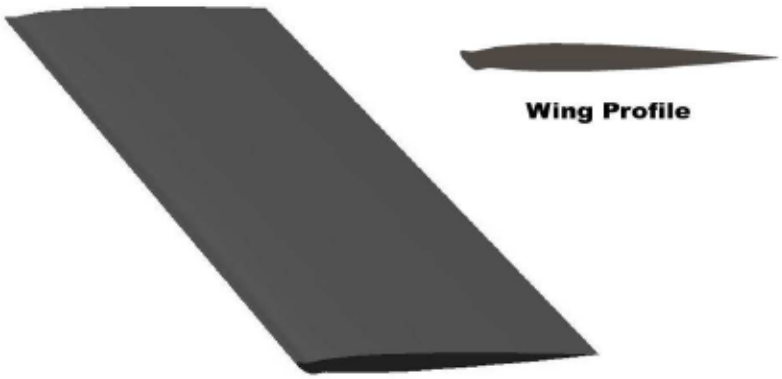

Figure 1.7: Swept wing with NACA 0012 airfoil section with glaze-ice shape

other, a swept wing configuration consists of a NACA 0012 airfoil section with a simulated glaze-ice accretion and a sweep angle of 30 degrees [4].

For the extruded wing problem, steady-state solutions of the RANS equations were carried out using CHEM and results were compared with corresponding RANS computations of Mogili [20] and also with experimental data. Hybrid RANS/LES computations were carried out using CHEM with the SST turbulence model [25]. Results were then compared with corresponding DES computations of Mogili [20] and with experimental data. For the swept wing configuration, RANS and hybrid RANS/LES computations were carried out using CHEM and results compared with the experimental data.

1.4 Outline of the thesis

Chapter II summarizes the literature on relevant experimental and computational studies and including the application of DES to wings with ice accretion. Chapter III focuses on issues associated with turbulence modeling using hybrid RANS/LES and also briefly describes the workings of CHEM. The geometry

modeling, mesh considerations, and mesh generation techniques are discussed in some detail in Chapter IV. Chapter V presents the results and comparisons with experimental data for both the extruded wing as well as the swept wing case. The results are discussed along with their implications. Conclusions drawn from the present e ort and recommendations based thereupon are presented in Chapter VI.

CHAPTER II

LITERATURE REVIEW

2.1 Introduction

Although studies of ice accretion and its e ects on aerodynamics began in the late 1920's and early 1930's, serious e orts were not initiated until World War II. During this period, icing tunnels became operational with a focus on measuring the e ects of ice accretion on lift and drag. Icing research was largely experimental although some attempts to analytically relate aerodynamic e ects to ice accretion were made [10]. The period after 1978, with the initiation of research at the (then) NASA Lewis Research Center, is considered to be the period of modern aircraft icing research [10]. The focus largely remained on understanding the e ects of ice accretion on the lift and drag of airfoils as well as on overall aircraft performance.

Computational Fluid Dynamics (CFD) began to come into prominence in the icing research arena with the initiation of the NASA aircraft icing program in 1979 [10]. Supporting experimental studies were performed on airfoils and wings to provide detailed aerodynamic data for the validation of the various CFD techniques. Early CFD research focused on flows about NACA 0012 airfoils with large glaze-ice horns. In the early 1990's, the focus shifted from large ice accretions to interest in frost roughness e ects on airfoil and wing aerodynamics. With the ATR-72 accident in 1994 [10], research on aircraft icing and its e ects was diversified to include studies on various types of ice accretions and other airfoil

sections and their respective sensitivities to icing. Computational e orts also received a major boost with several joint research programs for code development and validation. The di erent airfoil sections considered included the NACA 23012, NLF 0414, GLC 305 and NACA 6 series airfoils, which are representative of the airfoils that are presently used in general aviation and commercial transport fleets.

2.2 Experimental studies

The Icing Research Tunnel (IRT) was built between 1942 and 1944 at the NACA Lewis Research Center [10]. A significant number of the reported experimental studies have utilized the IRT. Continuous improvements and modifications have been made to the facility through the years to meet changing research requirements. Now, the IRT is an atmospheric closed-loop refrigerated wind tunnel capable of operating at temperatures as low as -40 F [5]. Airspeeds as high as 430mph can be attained in the 6-ft-high by 9-ft-wide by 20-ft-long test section. Figure 2.1 shows an aircraft wing model with ice accretion in the IRT. During its early days, tests in the tunnel were aimed at documenting the changes in airfoil performance characteristics due to ice accretion and also serving as a test bed for new de-icing and anti-icing systems.

After 1978, with the commencement of the icing research workshop at NASA, experimental icing research focused on acquiring data to aid CFD studies. Correlations of experimental measurements were made to provide empirical methods to estimate the e ects of ice on aircraft performance. Bragg [26] correlated drag rise for rime-ice and glaze-ice accretions. Bragg and Coirier [27] used a split-film probe to measure velocity characteristics within a separation bubble aft of a simulated glaze-ice horn on NACA 0012 airfoil. These results revealed a large

Figure 2.1: Iced aircraft wing in icing research tunnel [4]

recirculation region growing in chordwise extent with increasing angle of attack until it reached maximum lift after which the region failed to reattach and the lift decreased. Laser Doppler Velocimeter (LDV) measurements by Bragg and Khodadoust [28] were performed to further the knowledge about the unsteady characteristics of this bubble region. Kerho [29] performed detailed hot wire studies of the boundary layer development downstream of large distributed roughness located near the airfoil leading edge.

Bragg *et al.* [7] conducted LDV studies on a semi-span wing of e ective aspect ratio five with a simulated glaze-ice accretion. The model, a NACA 0012 airfoil section on a rectangular, untwisted planform, was mounted from the sidewall of the University of Illinois at Urbana-Champaign subsonic wind tunnel. Two configurations were tested: a zero sweep configuration and a 30-degree sweep configuration. The flow velocity was measured using a four-beam two-color fiber optic LDV. The velocity field observed along the centerline of the unswept wing compared well with experimental measurements on a similar two-dimensional model. A large leading-edge vortex was observed in the swept wing flow field which sweeps o the trailing edge before reaching the wing tip. Complicated flow was also observed downstream of the wing tip with the interaction of wing tip vortex and the leading-edge vortex. Experimental studies on large glaze-ice shapes continued with three-dimensional iced wing flow fields being studied in the mid 1990's [10].

With the initiation of the modern airfoils program by NASA Lewis Research Center and the FAA William J. Hughes Technical Center, a database of ice shapes and their respective aerodynamic performance was obtained [10]. As a result of these e orts, and with the identification of a vertical spanwise-ridge ice accretion, several aerodynamic studies were initiated to investigate the performance degradation due to this form of ice accretion. Addy *et al.* [30]

investigated Supercooled Large Droplet (SLD) ice-accretions on a NACA 23012 wing section having a slight taper. Lee and Bragg [31], [32] used a forward-facing quarter-round geometry to simulate ridge ice based on the icing-tunnel tests of Addy *et al.* [30]. Tests were performed on a two-dimensional NACA 23012 airfoil model at Re=1.8x10^6 and M = 0.18. A significant reduction in maximum lift coefficient was observed with the formation of a long separation bubble downstream of the simulated ice shape at certain critical chordwise locations. Similar tests were done on a NLF 0414 airfoil by Lee and Bragg [32]. $C_{l_{max}}$ values were found to be as low as 0.27 for the NACA 23012 airfoil. The NLF 0414 $C_{l_{max}}$ did not reach such low levels but varied around 0.7 to 0.8. These parametric studies provided insights into the e ects of ice-shape size and location on di erent airfoil geometries.

Papadakis *et al.* [33] investigated the e ects of glaze-ice shapes on the aerodynamic performance of a NACA 0011 airfoil section. Ice shapes were simulated with thin flat plates (spoiler-ice) extending along the span of the wing, and was used to simulate both the upper and lower surface horns. Aerodynamic tests were carried out at the NASA Langley Low-turbulence Pressure Tunnel (LTPT) by Addy *et al.* [34] to obtain high-quality aerodynamic data over a large range of Reynolds and Mach numbers. Gurbacki *et al.* [3] investigated the flow about a NACA 0012 airfoil with simulated three-dimensional and two-dimensional leading-edge glaze-ice accretions. They observed a low-frequency flow phenomenon on the order of 10 Hz that resulted in Strouhal numbers in the range 0.0048-0.0101. These oscillations produced large scale pressure fluctuations near separation at higher angles of attack. A separation bubble of varying thickness with a fluctuating reattachment location was also observed downstream of the ice accretion.

Wind tunnel tests were conducted by Addy *et al.* [5] in the LTPT to study the aerodynamic e ects of various ice accretions on the aerodynamic performance

of a two-dimensional business jet airfoil. The GLC 305 airfoil with a 944-glaze-ice shape [5] was chosen as the two-dimensional profile. The Reynolds number ranged from $3.0\text{x}10^6$ to $10.5\text{x}10^6$ and the Mach number ranged from 0.12 to 0.28. For the 944-glaze-ice configuration, the reduction in maximum lift coefficient was as high as 48%. For the conditions considered, Reynolds number e ects were more pronounced than Mach number e ects. Broeren *et al.* [6] carried out further studies on the upper surface of this GLC 305 airfoil with simulated glaze and rime ice shapes. A split-hot-film probe provided the mean streamwise and vertical velocities and the root-mean-squared fluctuations of the streamwise velocity at several chordwise locations. Measurements were made for Re=$3.5\text{x}10^6$ and Re=$6.0\text{x}10^6$ at Mach numbers of 0.12 and 0.21. A large separation bubble was observed downstream of the ice shape in both cases with the separation bubble for the glaze-ice-shape significantly larger than that for the rime ice-shape.

2.3 Computational Studies

With the initiation of the aircraft-icing program in 1979, there was a wider use of computational techniques as part of the studies on aircraft icing. Experimental research continued in parallel with the computational studies with the added responsibility of providing detailed data for CFD code validation.

2.3.1 Reynolds Averaged Navier-Stokes (RANS) Simulations

In 1985, Potapczuk [35] used a thin-layer, Reynolds-Averaged Navier Stokes (RANS) method to compute the flow field about a NACA 0012 profile with glaze-ice accretion configuration. Cebeci *et al.* [36] used an interacting boundary layer technique for similar geometries with ice accretions. Three-dimensional RANS

computations, undertaken by Kwon and Sankar [37] in 1990, were made possible by the availability of increased computational power. By this time, with improvements in turbulence modeling and grid generation, interacting boundary layer techniques were replaced by more sophisticated Navier Stokes calculations. Potapczuk and Sankar [38] performed three-dimensional RANS calculations on straight and swept wings with simulated glaze-ice accretions. These results revealed a strong leading-edge vortex with significant spanwise velocity in the core brought about by the flow separation from the glaze-ice-shape on the swept wing. These results obtained using computational methods compared well with corresponding experiments done by Bragg *et al.* [7].

Dunn *et al.* [39] carried out an integrated experimental and computational study to determine the e ect of simulated ridge ice shapes on airfoil aerodynamics on a modified NACA 23012 (23012m) airfoil and a NLF 0414 airfoil at Reynolds numbers of $1.8x10^6$ for a range of ice shapes at di erent chordwise locations on the airfoil. A solution-adaptive unstructured mesh was utilized to run steady-state simulations with a RANS solver. There was a reasonable agreement between the computational and experimental results for a wide range of experimental conditions. Two-dimensional and three-dimensional Navier Stokes computations were carried out by Chung *et al.* [40] to study the performance degradation associated with ridge-ice contamination on the wing of a commercial turbo-prop powered aircraft. Grid sensitivity studies were undertaken and the authors concluded that the work showed that grid resolution was an important factor in computing these types of flows and that a sensitivity analysis was important in obtaining a grid-independent solution.

Computational studies were performed for NLF 0414 airfoil with 6 and 22.5 minute ice accretions, and results were compared with data obtained at the LTPT

at NASA Langley [41]. Lift characteristics for Reynolds numbers ranging from $3x10^6$ to $10x10^6$ and Mach numbers ranging from 0.12 to 0.29 were compared and it was seen that the predicted stall angles were in agreement with experiment, within one or two degrees. Comparisons were made between results computed using the S-A turbulence model [42] and the SST turbulence model [25] to document the ability of each to predict the aerodynamic coefficients. It was found that, while the SST model performed better than the S-A model for the 6 minute ice, the S-A model showed better results for the 22.5 minute ice. Dunn and Loth [43] and Kumar and Loth [17] computed the e ects of simulated spanwise ice shapes on airfoil aerodynamics using RANS simulations. Recently, Pan and Loth [19], carried out RANS simulations over a range of Reynolds numbers and Mach numbers, for various ice-shape sizes and locations. The airfoils that were considered were the NACA 23012, the NLF 0414, and the NACA 3415 airfoils. Up to the stall condition, comparisons between the simulated results and experimental force data were favorable. At and after stall, strong separation occurs and aerodynamic forces were not predicted accurately for large upper-surface ice shapes.

2.3.2 Detached-Eddy Simulations (DES)

Many complexities arise when predicting the flow over an iced airfoil. The boundary layer separation over the ice shape, the presence of a separation bubble behind the ice shape, near-stall aerodynamics, reattachment of flow over the body at lower angles of attack and non-attachment of the flow at higher angles of attack are some of the physical phenomena that pose difficulties. All the above may lead to an unsteady flow field, which contributes to simulation complexity.

DES was first applied to iced airfoils in 1999 by Kumar and Loth [16]. A NLF 0414 airfoil having an ice shape with a height of 6.67% of its chord located

at the leading-edge was simulated at various angles of attack using DES and the results obtained matched adequately with a previous RANS simulation [17]. Grid resolution and time step e ects were examined using two-dimensional time-accurate simulations. Three-dimensional simulations were then performed at angles of attack of 5° and 7° and they showed improvement relative to RANS simulations in terms of C_l (comparisons were based on the experimental value). Although there was a discrepancy in the value of C_l, this was attributed to the the grid being too coarse. Their work on DES was motivated by the earlier results of Spalart *et al.* [18] in the three-dimensional simulation of a clean NACA 0012 profile at high angle of attack. The confidence gained from the above e orts laid the groundwork for additional work on iced airfoils using DES by Pan and Loth [11]. Prediction of stall and near-stall aerodynamics was the main aim. The three-dimensional DES study was carried out on a NACA 23013 airfoil at Re=2.0x10^6 and M = 0.21. The unsteady flow field associated with separation was captured qualitatively using the DES simulations. The maximum lift coefficient was found to be consistent with the experiments, whereas RANS simulations failed to predict the maximum lift coefficient. It was also observed that, in general, DES computations compared better with experimental data than RANS simulations.

The simulations that provide the motivation for this work were performed by Mogili [20] and Mogili *et al.* [21] on an extruded wing with a GLC 305/944-ice shape cross-section and a rectangular planform using the DES technique with the one equation Spalart-Allmaras model. Mogili [20] and Mogili *et al.* [21] employed the AVUS code [22] to compute steady-state RANS solutions and DES solutions. These numerical results were evaluated by comparison with the lift and drag data obtained by Addy *et al.* [5] and flow velocity data obtained by Broeren *et al.* [6]. Three-dimensional DES computations showed some improvement over

RANS simulations when compared to experimental data near stall angle of attack. The length and position of the separation bubble formed aft of the ice-shape was seen to be overestimated and the separation region had been shifted aft of the experimental location.

2.4 Summary

This review of experimental and computational studies on aircraft wings with ice accretions reveals the complexity of the flow field. Capturing the resulting unsteadiness requires modeling unsteady vortex and shear layer dynamics using temporally and spatially accurate calculations. The flow over an iced aircraft wing has many of the characteristics of a high angle of attack flow, even though the wing may be flying at a low angle of attack. This is particularly true for glaze-ice accretions which may form horns near the leading-edge. The review reveals the shortcomings of conventional RANS simlulations to e ectively capture the unsteadiness associated with flow over wings with ice accretion and in general for flows with massive separation. In contrast, hybrid RANS/LES approaches, such as DES, show promise for predicting these complex unsteady flow fields.

CHAPTER III

METHODOLOGY AND FLOW SOLVER

3.1 Hybrid RANS/LES Approach

A large majority of the CFD simulations for flows at high Reynolds numbers are obtained using RANS turbulence models. Although these models yield predictions of useful accuracy for attached flows, they fail to capture satisfactorily the unsteadiness associated with complex flows. These unsteady separated flows are substantially di erent from the thin shear layer and attached boundary layer flows that are used to calibrate the RANS models. In many engineering problems, the ability to predict separated flows is of great importance. Inferences drawn from the literature review reported in Chapter II highlight the shortcomings of RANS in predicting these complex separated flows.

Alternatives to RANS for predicting such separated flows include Direct Numerical Simulation (DNS) [12] and Large Eddy Simulation (LES) [12]. In DNS, the entire range of spatial and temporal scales of the turbulence are resolved and the Navier-Stokes equations are numerically solved without using a turbulence model. Even at low Reynolds number, the computational cost for DNS is exhorbitant, which makes DNS not feasible for realistic problems with currently available computational power. In LES, the large eddies are computed while the smallest, subgrid-scale (SGS) eddies are modeled based on the premise that it is the largest eddies that are directly a ected by the geometry and boundary conditions

and carry most of the Reynolds stress. Even though the computational cost of LES is significantly lower than DNS, the application of LES to high Reynolds number flows like aircraft wings with ice accretion is still not practical [13]. For high Reynolds number flows, the grid resolution required for attached boundary layers is very fine because the dominant eddy structures near the wall are extremely small and this grid requirement makes the computation prohibitively expensive.

Hybrid RANS/LES is a relatively new approach aimed at predicting complex separated turbulent flows at high Reynolds numbers at manageable cost. It combines the fine-tuned RANS simulation in the attached boundary layers with the power of LES in the shear layers and separated regions. Spalart *et al.* [13] originally proposed DES, a hybrid RANS/LES approach, as *" .... a new , hybrid simulation strategy, which was prompted by our LES cost estimate and by the modest but growing literature on unsteady modeled turbulence simulations."* Spalart *et al.* [13] defines the classical description of eddies internal to the boundary layer as "attached" eddies and ones in the separated region as "detached" eddies. Spalart *et al.* proposed resolving the detached eddies while modeling the attached ones.

DES, as initially proposed by Spalart [13], employs the one-equation Spalart-Allmaras turbulence model. Subsequently, Nichols *et al.* [14] implemented a multiscale $k-\epsilon$ model. The SST formulation, as implemented in CHEM [23, 24], has been used in simulations in the current e ort.

3.2 The Flow Solver: CHEM

The viscous flow solver, CHEM [23, 24], is implemented in the Loci [44] rule-based computational framework. The Loci framework assembles the numerical simulation components into a problem-oriented solver using a rule-based approach

to enhance flexibility and to reduce complexity of the CFD software employed. The CHEM code is a library of Loci rules (fine-grained components) providing primitives for general mesh elements, operators such as gradient, inviscid flux functions and transport functions, a variety of time and space integration methods, linear system solvers and more [23].

3.2.1 Governing Equations

The flow equations are discretized using a finite-volume approach. After integration over a computational cell, the governing equations for a three-dimensional flow with non-equilibrium chemistry and equilibrium internal energy, written in vector form for an arbitrary control volume $_c$ (closed by a boundary $\partial\ _c$) are [24]:

$$\frac{d}{dt}\int_{c(t)} Q\ dV + \int_{\partial\ c(t)} (F_i - F_v)\ dS = \int_{c(t)} \dot{W}\ dV, \tag{3.1}$$

where the vectors of conservative state variables, Q, inviscid flux, F_i, viscous flux, F_v, and chemistry source term, $\dot{W}$, are given by:

$$Q = \begin{bmatrix} \rho_1 \\ \vdots \\ \rho_s \\ \vdots \\ \rho_{\mathbf{NS}} \\ \rho\tilde{u} \\ \rho e_0 \end{bmatrix}, \quad F_i = \begin{bmatrix} \rho_1 \tilde{u}\cdot\tilde{n} \\ \vdots \\ \rho_s \tilde{u}\cdot\tilde{n} \\ \vdots \\ \rho_{\mathbf{NS}} \tilde{u}\cdot\tilde{n} \\ (\rho\tilde{u}\tilde{u} + p\tilde{\tilde{I}})\cdot\tilde{n} \\ (\rho e_0 + p)\,\tilde{u}\cdot\tilde{n} \end{bmatrix}, \tag{3.2}$$

$$F_v = \begin{bmatrix} -\rho_1 \tilde{V}_1 \cdot \tilde{n} \\ \vdots \\ -\rho_s \tilde{V}_s \cdot \tilde{n} \\ \vdots \\ -\rho_{\mathbf{NS}} \tilde{V}_{\mathbf{NS}} \cdot \tilde{n} \\ \tilde{\tilde{\tau}} \cdot \tilde{n} \\ (\tilde{u} \cdot \tilde{\tilde{\tau}} - \tilde{q} - \sum \rho_s h_s \tilde{V}_s) \cdot \tilde{n} \end{bmatrix}, \quad \dot{W} = \begin{bmatrix} \dot{w}_1 \\ \vdots \\ \dot{w}_s \\ \vdots \\ \dot{w}_{\mathbf{NS}} \\ 0 \\ 0 \end{bmatrix}. \tag{3.3}$$

In flows with no chemical reactions and only a single species, like the problems treated in this e ort with air as the only species, the source term in the governing equation is zero.

3.2.2 SST Turbulence Model

Several turbulence models, including the SST formulation of Menter [25], have been implemented in CHEM. The SST turbulence model, based on Menter's baseline model, is a good general purpose model that is reasonably e ective at predicting flow separations [23].

The defining equations for the SST model are written as:

Kinematic Eddy Viscosity:

$$\nu_t = \frac{a_1 k}{\max(a_1 \omega, \quad F_{sst})}, \tag{3.4}$$

where is the absolute value of the vorticity. F_{sst} is given by:

$$F_{sst} = tanh(arg_{sst}^2) \tag{3.5}$$

$$arg_{sst} = \max\left(2\frac{\sqrt{k}}{0.09\omega y}, \frac{500\nu}{y^2\omega}\right) \tag{3.6}$$

where y is the distance to the closest point away from the wall surface.

Turbulent Stress Tensor:

$$\tau_{ij}^{'} = \mu_t \left(\frac{\partial u_i}{\partial x_j} + \frac{\partial u_j}{\partial x_i} \right) - \frac{2}{3} \left(\mu_t \nabla \cdot \tilde{u} + \rho k \right) \delta_{ij}, \quad i = 1, 2, 3, \quad j = 1, 2, 3, \tag{3.7}$$

Turbulent Kinetic Energy Equation:

$$\frac{D\rho k}{Dt} = \tau_{ij}^{'} \frac{\partial u_i}{\partial x_j} - \beta^{\star} \rho \omega k + \frac{\partial}{\partial x_j} \left[(\mu + \mu_t \sigma_k) \frac{\partial k}{\partial x_j} \right], \tag{3.8}$$

Turbulent Dissipation Equation:

$$\frac{D\rho\omega}{Dt} = \frac{\gamma}{\nu_t} \tau_{ij}^{'} \frac{\partial u_i}{\partial x_j} - \beta \rho \omega^2 + \frac{\partial}{\partial x_j} \left[(\mu + \mu_t \sigma_\omega) \frac{\partial \omega}{\partial x_j} \right] + 2(1 - F_{sst}) \rho \sigma_{\omega 2} \frac{1}{\omega} \frac{\partial k}{\partial x_j} \frac{\partial \omega}{\partial x_j}. \tag{3.9}$$

Closure Coefficients:

All the constants ϕ of the model are computed by blending the appropriate $k - \omega$ and $k - \epsilon$ constants as follows:

$$\phi = F_{sst} \phi_1 + (1 - F_{sst}) \phi_2, \tag{3.10}$$

where the constants ϕ_1 $(k - \omega)$ are:

$$\sigma_{k1} = 0.5, \quad \sigma_{\omega 1} = 0.5, \quad \beta_1 = 0.075, \quad \beta^{\star} = 0.09, \quad \kappa = 0.41, \quad \gamma_1 = \beta_1 / \beta^{\star} - \sigma_{\omega 1} \kappa^2 / \sqrt{\beta^{\star}}, \tag{3.11}$$

and the constants ϕ_2 $(k-\epsilon)$ are:

$$\sigma_{k2} = 0.5, \quad \sigma_{\omega 2} = 0.856, \quad \beta_2 = 0.0828,$$
$$\beta^\star = 0.09, \quad \kappa = 0.41, \quad \gamma_2 = \beta_2/\beta^\star - \sigma_{\omega 2}\kappa^2/\sqrt{\beta^\star}. \quad (3.12)$$

To a ect transition from RANS to LES, a transfer function is used that, unlike the Spalart-Allmaras DES treatment, depends on both local grid spacing and turbulent flow properties [15]. In Spalart-Allmaras DES, the switching from RANS to LES depends only on the local grid spacing and not on the turbulent length scale. The SST model behaves like a LES subgrid model when the turbulent length scale is greater than the grid length scale [14]. The grid length scale is defined by:

$$L_G = max(\Delta x, \Delta y, \Delta z) \quad (3.13)$$

where Δx, Δy, Δz is the local mesh spacing in the x, y and z directions respectively. The turbulent length scale is defined by:

$$L_T = max(6.0\sqrt{\nu_{tRANS}/\ }, k_{RANS}^{3/2}/\epsilon_{RANS}) \quad (3.14)$$

where ν_{tRANS} is the unfiltered (large scale) eddy viscosity and is the local mean flow vorticity [14].

3.2.3 Spatial Integration

The numerical integration of the governing equation begins with the approximations to the volume and surface integrals. A second-order midpoint rule

is used for volume integrals. The numerical integration of the surface integrals is accomplished by summing the contribution of each face for a given cell [24].

The inviscid terms contained in the Navier-Stokes equations are treated using Roe's flux-di erence-splitting technique [24]. The Venkatakrishna limiter [45] is designed to allow small overshoots in relatively smooth regions, while strongly enforcing limiting where strong perturbations are present. Face values needed to evaluate the viscous fluxes are computed using a simple volume-weighted average of the integrated cell values on either side of the face. The face gradients consists of a combination of the average of the least squared gradient computed for the cells on either side of the face and gradient normal to the face. More details are continued in the CHEM user manual [24].

3.2.4 Time Integration

The equations governing fluid motion are highly nonlinear in nature due to the presence of the convection term in the momentum equation and also due to phenomena such as turbulence and chemical reactions [46]. Obtaining accurate numerical solutions for complex flows is challenging. To avoid direct solution of a large system of nonlinear equations, the governing equations are linearized about a provisional value of the solution and an iterative process is employed. Using an iterative scheme leads to an efficient matrix inversion with greatly reduced memory requirements. In practical problems with millions of grid points, direct matrix inversion has a prohibitively large memory requirement. Some iterative methods commonly used are the Jacobi method, Gauss-Seidel method, Successive Overrelaxation (SOR) method, and Symmetric Successive Overrelaxation (SSOR) method [47]. The iterative schemes employed in the present e ort are the Newton

iteration scheme and the Gauss-Seidel scheme wherein each Newton iteration consists of several Gauss-Seidel sub iterations.

The implicit time integration scheme in CHEM employs a two parameter family of algorithms and is given by the equation [23]:

$$\begin{aligned} &\mathcal{V}((1+\psi)\Delta Q^n - \psi \Delta Q^{n-1}) = \\ &\Delta t\{(1-\theta)R^n(Q^n) + \theta R^{n+1}(Q^{n+1})\}, \end{aligned} \tag{3.15}$$

where R is the residual term, which includes all source terms and fluxes, n is the current time step, and $\Delta Q^n = Q^{n+1} - Q^n$. In this scheme, θ and ψ form a two parameter family of algorithms. Setting $\theta = 1, \psi = 0$ gives the implicit backward Euler scheme typically used in steady state simulations, while a second-order three point backward scheme ($\theta = 1, \psi = \frac{1}{2}$) is used for time-accurate simulations.

Equation (3.15) represents a non-linear system of equations for the values of Q^{n+1}, and can be rearranged as:

$$\begin{aligned} \mathcal{L}(Q^{n+1}) =& \mathcal{V}(Q^{n+1} - Q^n) \\ &- \frac{\Delta t}{1+\psi}\left[(1-\theta)R^n(Q^n) + \theta R^{n+1}(Q^{n+1})\right] \\ &- \mathcal{V}\frac{\psi}{1+\psi}(Q^n - Q^{n-1}) \\ &= 0. \end{aligned} \tag{3.16}$$

Equation (3.16) is solved by a Newton iterative method, as follows:

$$\mathcal{L}'(Q^{n+1,p})(Q^{n+1,p+1} - Q^{n+1,p}) = -\mathcal{L}(Q^{n+1,p}), \tag{3.17}$$

where p is an iteration counter. The Newton iteration is initialized using the value at the previous time step ($Q^{n+1,p=0} = Q^n$) and the Jacobian $\mathcal{L}'(Q^{n+1,p})$ is given by

$$\begin{aligned}\mathcal{L}'(Q^{n+1,p}) &= \frac{\mathcal{V}^{n+1}(1+\psi)}{\theta\Delta t} I - \left[\frac{\partial}{\partial Q} R^{n+1,p}(Q)\right] \\ &= \frac{\mathcal{V}^{n+1}(1+\psi)}{\theta\Delta t} I - \mathcal{V}^{n+1}\frac{\partial \dot{W}}{\partial Q} \\ &+ \sum_{f\in faces} \mathcal{A}_f^{n+1} \frac{\partial \hat{F}(Q_{l,f}, Q_{r,f})}{\partial Q} \\ &+ I \sum_{f\in faces} \mathcal{A}_f^{n+1} (\tilde{u}_{,f} \cdot \tilde{n}_f).\end{aligned} \tag{3.18}$$

Equation (3.17) is solved using a Gauss-Seidel iteration method [48]. The turbulent equations are solved decoupled from the flow equations and communication between the two is performed within each Newton step.

3.2.5 Preconditioning

Preconditiong is used to control the numerical dissipation associated with the solution of low Mach number flows. There is the large disparity between the acoustic wave speed and the fluid convection speed for low Mach number flows. Preconditioning methods alter the eigenvalues of the system of the compressible-flow equations so as to reduce the large disparity between the acoustic wave speed and fluid convection velocity.

A partially discretized version of the governing equations can be written as [49]:

$$_c\frac{\partial Q_c}{\partial t} = R_c, \qquad R_c = \ _cW_c - \oint_{S_c} (F)\cdot ndS, \tag{3.19}$$

where $_c$ is the control volume and R is the steady-state residual. After the preconditioned matrix, P, has been defined and introduced, Eq. (3.19) becomes:

$$ {}_cP_c^{-1}\frac{\partial Q_c}{\partial t} = R_c. \tag{3.20} $$

The global preconditioning matrix P, which does not depend on local flow conditions, is determined by the overall flow characteristic and is established by the choice of an appropriate reference Mach number. The diagonal matrix P is given by:

$$ P = diag\left\{1,\, 1,\, \ldots,\, \beta\right\}, \tag{3.21} $$

and the the inverse matrix P^{-1} is given by:

$$ P^{-1} = diag\left\{1,\, 1,\, \ldots,\, 1/\beta\right\}. \tag{3.22} $$

where the parameter β is a function of the reference Mach number. For simplicity, the parameter β can be chosen as follows:

$$ \beta = \begin{cases} \Pi_{20} & \Pi_{20} < 1, \\ 1 & \Pi_{20} \geq 1, \end{cases} \tag{3.23} $$

where Π_{20} is a non-dimensional energy ratio given as:

$$ \Pi_{20} = \left(U_r{}^2\right)^D / \left(e_{0,r}\right)^D \tag{3.24} $$

where U_r is the reference velocity and $(e_{0,r})$ is the reference internal energy. The superscript D denotes a dimensional value. β reduces to unity for $M_r \geq 1$ and hence the matrix P reduces to the identity matrix and no preconditioning is applied when $M_r \geq 1$.

CHAPTER IV

PROBLEM STATEMENT & PROCEDURES

The complex flow field associated with a wing with ice accretion makes computational prediction a daunting task. The boundary layer separates at the ice-shape and the flow reattaches aft of the accretion at low angles of attack while for higher angles of attack, the flow may not reattach [16]. The separation region aft of the ice-shape significantly complicates the aerodynamics and can lead to a highly unsteady flow field.

Once the configuration and flight conditions have been identified, the task of going about simulating such a flow consists of the following steps:

- Modeling the geometry using the given geometric parameters.
- Defining the computational domain by creating artificial boundaries for the flow domain as well as creating other artificial surfaces to control interior mesh spacing.
- Generating the surface mesh with the required spacings and setting the boundary conditions.
- Generating the three-dimensional volume mesh that defines the computational domain.
- Defining the various flow and algorithm parameters for the simulation.

- Simulating the flow.
- Post-processing and analyzing the results to obtain meaningful data.

The subsequent sections describe how the above steps were applied to the problems at hand in some detail.

4.1 Geometry Definition

Two di erent iced wing configurations were considered during this study. One was a constant-section, rectangular wing based on an extruded two-dimensional 944-glaze-ice shape on a GLC 305 airfoil section [4]. The other was a swept wing configuration with simulated ice on a NACA 0012 airfoil section with 30 degree sweep [7].

4.1.1 Extruded wing configuration with ice accretion

The first configuration is a rectangular planform wing on a business jet GLC 305 airfoil section. The rectangular planform was extruded from a 944-glaze ice accretion denoted as a two dimensional 944-glaze-ice shape as shown in figure 1.6. The GLC 305 airfoil was designed for low transonic drag and has a maximum thickness to chord ratio of 8.7%. The extruded wing has an aspect ratio of unity to match the configuration used in the test program [5, 6]. The wing employed for the test program was mounted between walls and therefore the geometry modeled in this study did not include wing tips. In this study, the conditions at which the flow was simulated are: M=0.12, Re/L=3.8x10^6/m which, with a chord length of 0.9144m, yields Re=3.5x10^6, and angles of attack of 4° and 6°. The flow conditions for the extruded 944-glaze-ice shape cases correspond to those in run 41 in the experimental data [4, 5].

4.1.2 Swept Wing Configuration With Ice Accretion

The swept wing configuration is a 30 degree swept semispan wing with a 5-minute simulated glaze ice accretion [7]. The wing has a NACA 0012 section perpendicular to the leading-edge. The wing model has a span of 35.18 inches and a chord of 17.32 inches. A simulated ice-accretion, based on icing results measured on a NACA 0012 airfoil in the NASA Icing Research Tunnel [50], was used. In this study, the conditions at which the flow was computationally simulated are: an angle of attack of 8° and a Re=3.5x10^6 to match the experimental data for comparison [7].

4.2 Mesh Considerations

The fact that both RANS and LES treatments have to be applied in the same field in a hybrid RANS/LES simulation adds to the complexity of mesh generation. Since separated flows and the geometries involved are inherently complex, assessing and comparing mesh performance pose problems too.

Spalart [51] gives comprehensive and to-the-point instructions and guidelines for mesh generation for a DES. Since resolution of hybrid RANS/LES computations also depends on the mesh, these guidelines were considered valid for general hybrid RANS/LES simulations and were adopted for meshes generated for the hybrid RANS/LES simulations undertaken as part of the current e ort.

Following Spalart [51], the flow field is divided into di erent regions so as to clearly define the meshing requirements in each region based on flow behavior. The flow field can be seen as being comprised of a RANS region, an Euler region (ER), an LES region, a Viscous Region (VR), an Outer Region (OR), a Focus Region (FR) and a Departure Region (DR). The first three regions are treated as “super

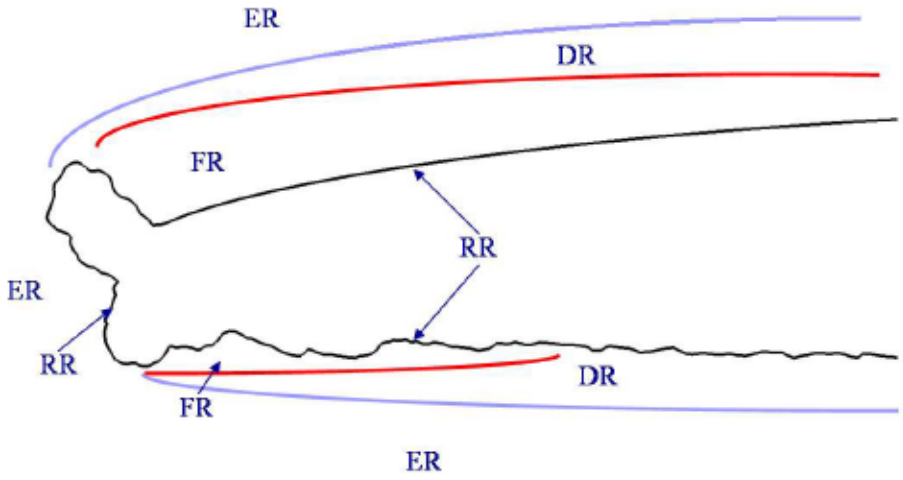

Figure 4.1: Estimated DES zones for iced wing with GLC 305 airfoil section with two dimensional 944-glaze-ice shape (extruded wing)

regions" encompassing the smaller regions as shown in Figure 4.1. This sketch can be used as a visual guide to understand the specific regions. Note that the viscous regions are too thin to be shown on the sketch. Also note that the regions are classified in terms of mesh considerations and not on the basis of the turbulence treatment.

4.2.1 Euler Region (ER)

In the problem of interest, the ER is mostly una ected by turbulence and vorticity. It covers the region far upstream and extends to infinity. It contains most of the volume of the mesh but contains a relatively small share of the points. Euler meshing practices are adopted here with isotropic tetrahedral elements.

4.2.2 RANS Region

The RANS region is primarily the boundary layer including the initial separation and also any shallow separation bubbles. Meshing practices typical

of pure-RANS calculations can be employed in this region. Refinement to a much finer mesh would activate LES in these regions.

The Viscous Region (VR) is a sub region inside the RANS region of a DES. The meshing requirements for the VR are the same as those for a full-domain RANS computation. As for a RANS mesh, the distance to the first point o the wall should be about $y^+ = 2$ or less. Spalart [51] also suggests the stretching ratio, $\delta y_{j+1}/\delta y_j$, should be around 1.25 or less for the log layer to be accurately resolved. The guide also suggests that RANS practices can be continued in directions parallel to the wall.

In the RANS Outer Region (OR), since there is no *LES content* (Spalart uses this term to identify the areas where unsteady three-dimensional eddies are present and thereby need to employ LES), the whole boundary layer is treated with modeled turbulence. RANS practices can be adopted for meshing normal to the wall.

4.2.3 LES Regions (LR)

Those regions that can be a ected by turbulence and vorticity at some point in the simulation can be classified as LES regions. The exceptions to this are the boundary-layer and thin shear layers.

This viscous region (VR) is inside the LES *super region* but the requirements in terms of meshing are basically the same as that of the RANS viscous region.

The Focus Region (FR) is the region close to the body where the turbulence must be resolved. For DES Spalart [51] defines a *target grid spacing* Δ_0 which should prevail throughout the focus region and goes on to state that Δ_0 *is the principal measure of spatial resolution in a DES* [51]. Chances of the occurrence of flow reversal at any point in the simulation can be used as indicator for roughly

identifying the streamwise extent of the FR. The main issue is to decide how far the FR should extend downstream so as not to lose efficiency by adding unnecessary mesh points.

The FR ends downstream of the separation and gives rise to the Departure Region (DR). In this region, the mesh resolution achieved in the FR is uncalled for and the value of Δ will far exceed the value of Δ_0 in the focus region. However, the transition from the FR to DR should be smooth. The DR meshing should smoothly give way to ER type meshing far downstream. The DR basically acts as a transition zone between the FR and the ER far downstream.

4.3 Mesh Generation

Mesh generation practices were in accordance with the guidelines proposed by Spalart [51] and described in section 4.2. The choice of whether to use a structured or an unstructured mesh is very problem specific. For problems like wings with complex ice-shapes, unstructured mesh generation is superior to structured grid generation. The user must define relatively complex block topology if a high quality structured grid is to be generated for a complex ice shape [52]. Unstructured mesh generation is usually a much less user intensive task. With respect to DES and hybrid RANS/LES simulations, there can be more control over the spacing of points in the focus region and near isotropy of mesh cells away from the surface can be achieved. Special considerations with regards to mesh generation for iced wings are:

1. Control of point spacings on the wing surface:
    - Point density near tips of horns

	# Nodes	# Faces	# Cells
Extruded Wing	2,394,393	22,088,508	10,579,834
Swept Wing	4,460,000	35,210,000	16,288,000

Table 4.1: Statistics for the meshes employed

- Point density near the trailing edge

2. Control of point spacing in isotropic tetrahedral mesh in the FR

3. Control of stretching in outer layers of the RR so spacing does not become too large to merge with the FR.

Table 4.1 shows the statistics for the two meshes employed in this e ort.

4.3.1 Extruded Wing Mesh

The extruded wing DES mesh was generated by Mogili *et al.* [20, 21] using VGridns [53] and GridTool [54]. VGridns employs the advancing-front method to generate tetrahedral volume meshes. VGridns allows reasonably good local mesh refinement through the use of "sources." Figure 4.2 shows the source distribution along the wing surface for the GLC 305 wing with 944-glaze-ice shape. Mesh refinement can be obtained by changing the strengths of these sources. Local mesh refinement in the FR on the extruded wing case was done by changing the source strengths in in the upper surface by a factor of two while holding the other sources constant. An average y^+ value of less than 0.5 was maintained for the extruded wing case. Mesh conversion into a compatible format was made possible using the Blacksmith utility [55].

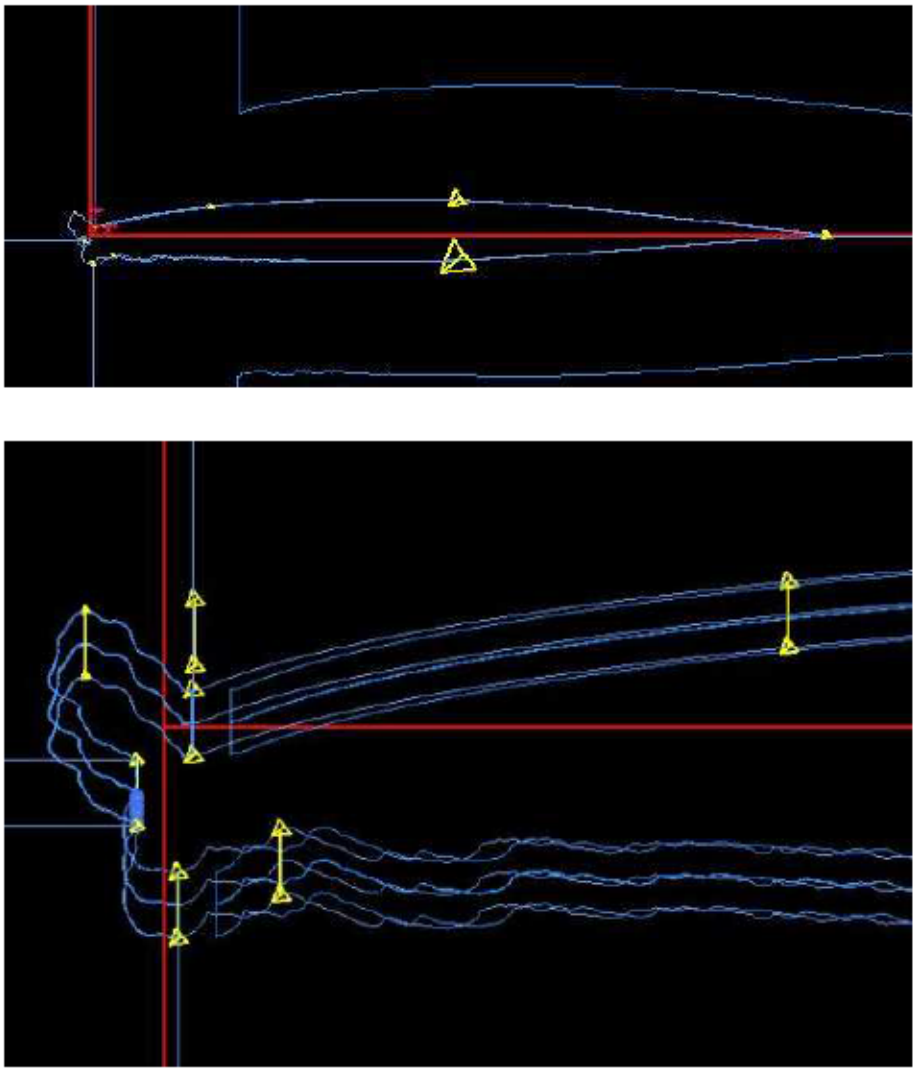

Figure 4.2: "Sources" used by GridTool/VGrid to generate mesh

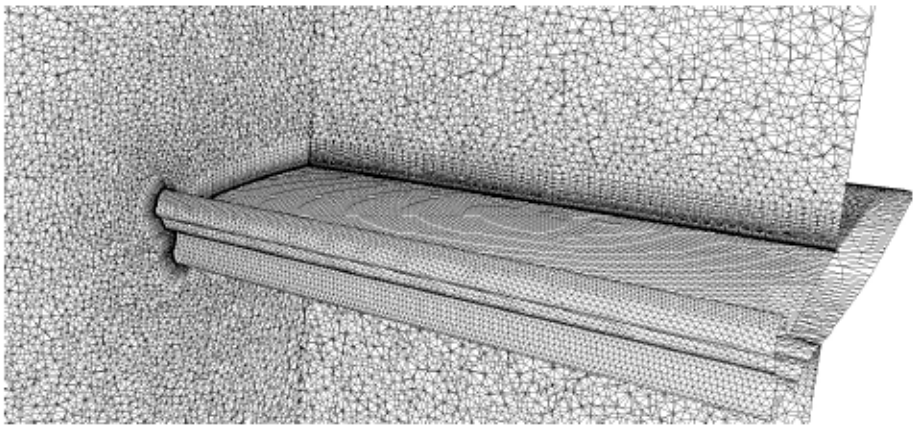

Figure 4.3: Mesh in cutting plane for aircraft wing with GLC 305 airfoil section (extruded wing)

4.3.2 Swept Wing Mesh Generation

Geometry modeling for the swept wing case was done using Solidworks [56]. Solidworks is a three-dimensional computer-aided design (CAD) program that runs on Microsoft Windows platforms. The coordinates of the wing/ice-accretion profile were input to Solidworks and the swept wing was generated according to geometry specifications given by Kerho *et al.* [50]. The output surface data was converted to the Initial Graphics Exchange Specification (IGES) format for input to the mesh generator.

Mesh generation for the swept wing case was performed using SolidMesh [57], a user interface to mesh generation tools AFLR2 and AFLR3 [57]. AFLR2/3 is based on the Advancing-Front/Local-Reconnection technique. Solidmesh also contains a CAD system based on Non-Uniform Rational B-Splines (NURBS) and a mesh visualization system. Point spacings in the three-dimensional domain were controlled using transparent artificial surfaces within the domain. A hierarchial control of point spacings from the wing surface outwards was achieved by the use of two transparent surfaces as shown in figure 4.4:

- A chord-length beyond the wing surface, the maroon surface shown in figure 4.4(a) helps to maintain a smooth transition from the fine spacings in the FR to the large spacings at the farfield.

- Encompassing the FR, the green surface shown in figure 4.4(b) tries to maintain the relatively close spacing required in this region.

A y^+ of unity has been maintained during mesh generation. Figure 4.5 shows the cross section of the swept-wing mesh at mid-span. Figure 4.6(a) gives an idea of the fine mesh spacings used on the wing surface and in the focus region as seen on the symmetry plane. Figure 4.6(b) shows a zoomed view of the wing surface very close to the tip. The two cutting planes also show the normal spacings of the prismatic cells near the wing surface.

4.4 Selection of Time Step Size

Spalart [42] laid out basic guidelines to determine the time-step for DES computations. The FR is where large eddies occur and it usually contains higher frequencies than other regions. The aim is to capture the smallest possible perturbations as well as higher frequency perturbations in the focus region by employing a time scale common to the whole flow. The eddies with wavelengths of around $\lambda = 5\Delta$ will be active. According to Spalart [42] *"even though they cannot be highly accurate because they lack the energy cascade to smaller eddies, and are under the influence of the eddy viscosity instead."* So, their transport using a di erencing scheme with $\Delta = \lambda/5$ may be acceptable. Their accuracy will also depend on the di erencing scheme. This leads to around five time steps per period and consequentially a CFL of unity. From this, we can deduce an approximate time

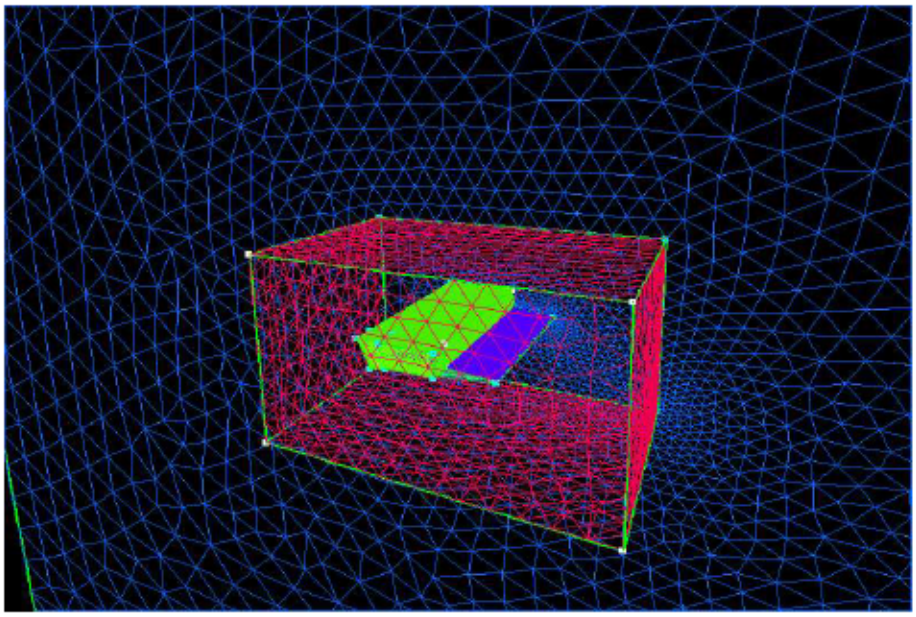

(a) The two transparent surfaces are shown in green and maroon

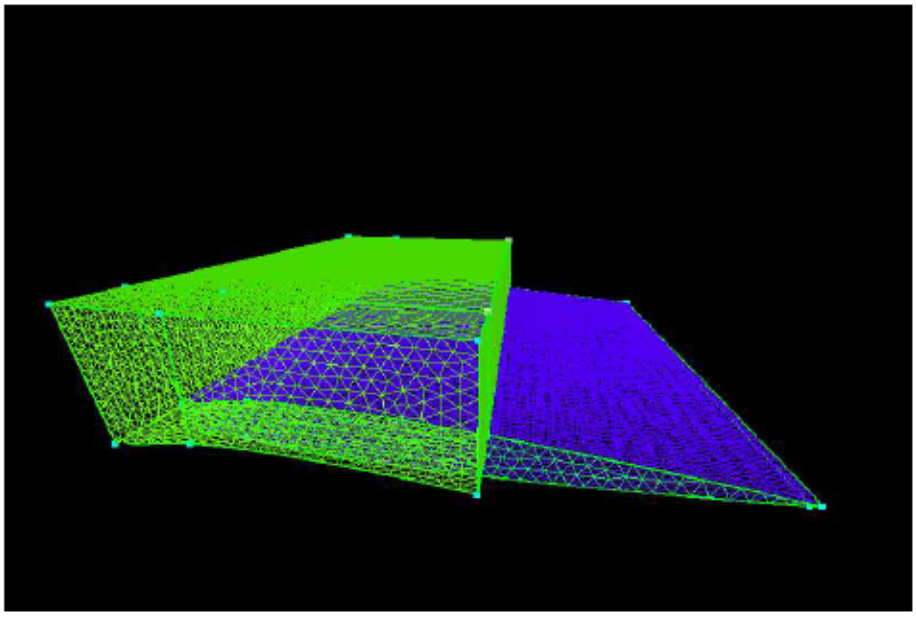

(b) The transparent surface to control mesh spacings in the FR

Figure 4.4: The transparent surfaces used to control spacings used by SolidMesh to generate the mesh

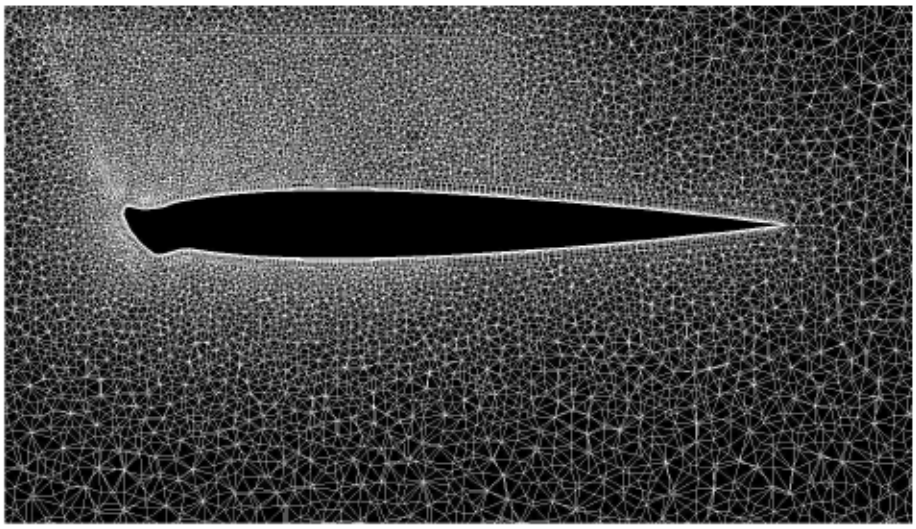

Figure 4.5: Swept wing mesh in cutting plane parallel to the flow

step value using $\Delta t = \Delta_0 / U_{max}$ where U_{max} is the magnitude of the maximum flow velocity encountered in the focus region.

For the extruded wing case, RANS results computed by Mogili [20] and Mogili *et al.* [21] indicate a maximum flow velocity over the domain to be about 40–50% greater than the freestream velocity. With a freestream velocity of approximately 41.1 m/s, the computation for time step size yields Δt_0=0.075ms as deduced by Mogili [20] and Mogili *et al.* [21]. For the swept wing case having a freestream velocity of approximately 35.7 m/s, a similar computation yields Δt_0=0.05ms.

4.4.1 Computational Resources

All cases reported in this e ort were run on 64 processors on the EMPIRE cluster or the MAVERICK cluster at the ERC at Mississippi State University [58]. EMPIRE is a 1038 processor Linux-based supercluster composed primarily of IBM xSeries x330 servers, each with two 1.266GHz or 1.0GHz Pentium III processors with 1.0 or 1.25 GB of memory. EMPIRE has a theoretical peak performance of 1.15 teraflops (trillion calculations per second) and a measured performance

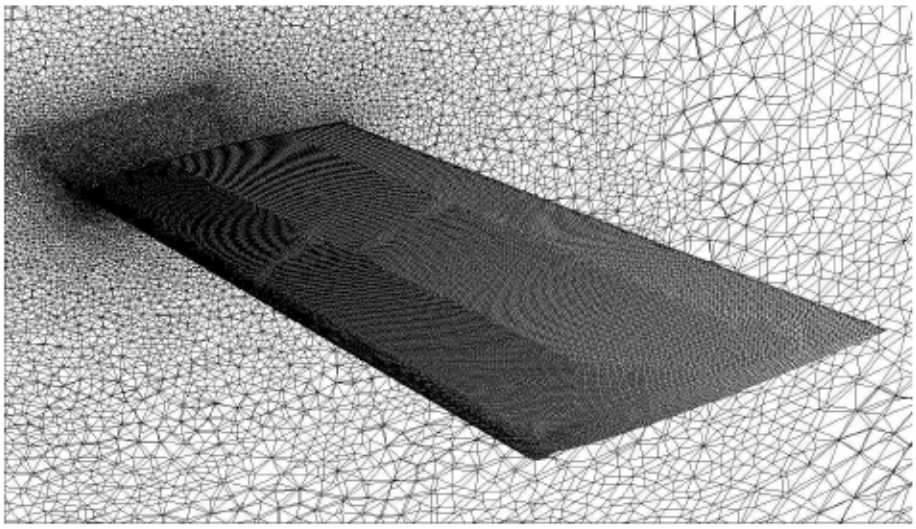

(a) The swept wing surface and symmetry-wall mesh

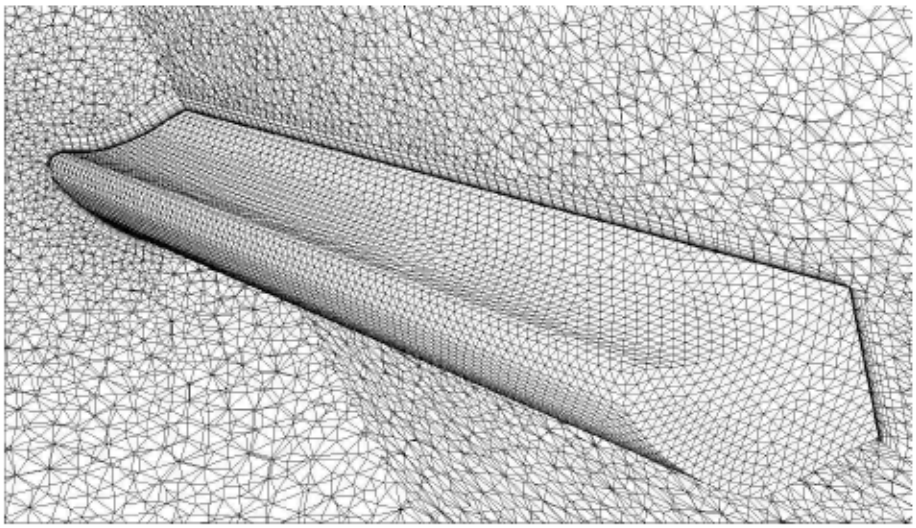

(b) A zoom-in view of the normal growth and the wing surface mesh close to the wing tip

Figure 4.6: Swept wing surface mesh

on the LINPACK benchmark of 366 gigaflops. MAVERICK is a 384 processor Linux-based supercluster composed of 192 IBM xSeries x335 servers, each with two 3.06GHz Xeon processors, and 2.5 GB of memory. MAVERICK has a theoretical peak performance of 2.35 teraflops and a measured performance on the LINPACK benchmark of nearly 1.4 teraflops.

CHAPTER V

RESULTS & DISCUSSION

A detailed discussion and analysis of RANS and hybrid RANS/LES results computed using CHEM are presented for the extruded wing configuration (GLC 305 with 944-glaze-ice shape [4]) and the swept wing configuration [7]. In Section 5.1, the results of the RANS and hybrid RANS/LES simulations performed for the extruded wing configuration are presented and compared with the DES results of Mogili [20] and Mogili *et al.* [21] and with the corresponding experimental data [5, 6]. In Section 5.2, the details of the RANS and hybrid RANS/LES simulations performed for the swept wing configuration are presented and compared with the experimental data of Bragg *et al.* [7]. Subsections organized within each section discuss the experimental data, the RANS results, and the hybrid RANS/LES results. In Section 5.3, the results computed for the extruded wing configuration and swept wing configuration is summarized and the implications of the results are discussed.

5.1 Extruded Wing Configuration

5.1.1 Experimental Details

Wind tunnel tests were conducted by Addy *et al.* [5] in the LTPT at NASA Langley to study the e ects of various ice accretions on the aerodynamic performance of a 36-inch chord, two-dimensional business jet airfoil (GLC 305).

The GLC 305 airfoil is designed for low transonic drag and has a maximum thickness to chord ratio of 8.7%. The two-dimensional model, designed with removable leading edge, had a 36-inch chord and a 36-inch span. A clean wing configuration and configurations with extruded ice shapes were studied. One of the ice shapes considered was the 944-glaze-ice shape, which is the ice shape of interest in the present e ort.

The airfoil model was supported horizontally across the width of the test section between two 40-inch diameter circular end-plates. These end-plates were flush mounted with the sidewalls and rotated to adjust the angle of attack. Each end-plate contained a porous section for sidewall boundary layer control. The Reynolds number ranged from 3.0×10^6 to 10.5×10^6, while the Mach number ranged from 0.12 to 0.28. The lift and pitching moment data were obtained by integrating the surface pressures, while the drag coefficients were calculated using the standard momentum deficit method based on the pressures measured using a wake probe. Corrections to the integrated performance coefficients accounting for solid and wake blockage and streamline curvature were applied to the data during post processing.

Comparisons between the lift and drag coefficients for the clean wing and the extruded wing are shown in Figures 5.1(a) and 5.1(b). Figure 5.1(a) shows that a reduction in the lift coefficient for the extruded wing can be observed at all angles of attack when compared to the clean wing configuration. The reduction in lift becomes more significant at "near stall" angles of attack. Figure 5.1(b) shows a significant increase in the drag coefficient for the extruded wing configuration when compared with the clean wing configuration that grows dramatically at "near stall" angles of attack.

The pressure coefficient distributions for the clean wing and the extruded wing for angles of attack of 4° and 6° are shown in Figure 5.2. For the extruded wing

configuration, the pressure coefficient distribution shows a constant pressure region on the upper surface that extends from the leading edge to about $x/c \approx 0.16$ for the 4° case and to about $x/c \approx 0.3$ for the 6° case. This constant pressure region is indicative of flow separation and bubble formation on the upper surface aft of the ice shape. In the 6° case, the extruded wing pressure is shifted upward relative to the clean wing. The cause of this behavior is not known.

Broeren *et al.* [6] obtained detailed flow field measurements on the upper surface of the extruded wing with 944-glaze-ice shape [4]. Split-hot-film anemometry was used to determine the streamwise and vertical velocity profiles at several chordwise locations along the upper surface at the midspan. The time-averaged flow velocities and RMS of the fluctuations in the streamwise velocity component were measured. The data were obtained at Reynolds numbers of 3.5×10^6 and 6.0×10^6 corresponding to Mach numbers of 0.12 and 0.21. Figure 5.3 shows the time-averaged streamwise velocity plots for the extruded wing at two angles of attack preceding stall. These images provide a good illustration of the flow aft of the ice shape. The reattachment location of the upper surface flow may be estimated by locating the position on the chord at which the contour u=0 (light blue) intersects the upper surface of the wing. This visual guide is applicable to all the streamwise velocity images presented in this thesis. Separation occurs near the tip of the glaze ice horn and a significant reversed flow region, indicative of a separation bubble, can be seen aft of the ice shape for both the 4° and 6° angles of attack. Reattachment is seen to occur at about 30% chord at 4° angle of attack and at about 50% chord at 6° angle of attack.

Figure 5.4 shows the RMS of the fluctuations in the streamwise velocity component for the 4° and 6° cases. From Figures 5.3 and 5.4 it can be seen that on the upper surface, the shear layer becomes unstable soon after separation

making the flow downstream highly unsteady. The region where the RMS of the fluctuations in the streamwise velocity is maximum is nearer to the ice shape at 4° angle of attack when compared to the 6° case. For the 6° case, the region where the RMS is maximum is near mid-chord and this region is thicker and extends further downstream when compared to the 4° case.

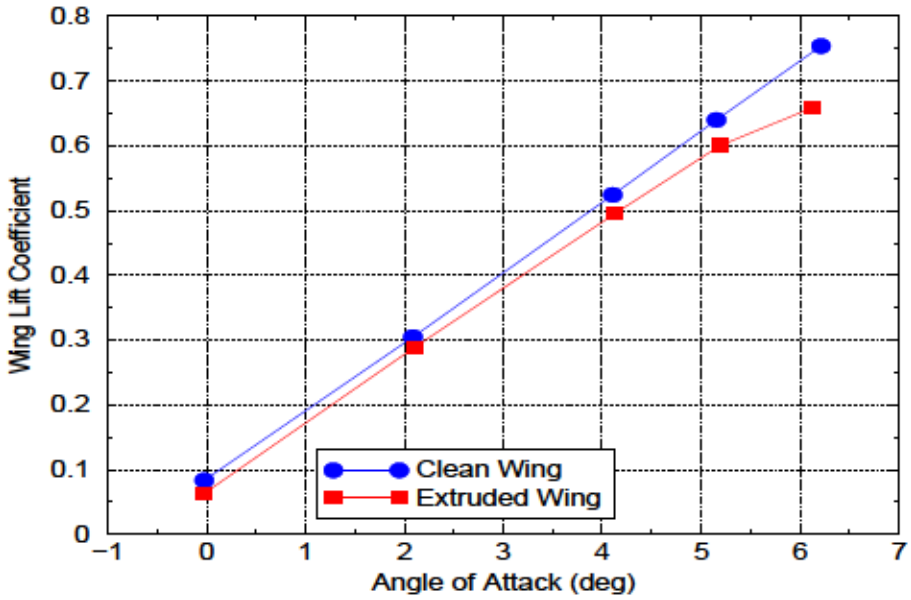

(a) Experimental lift coefficients

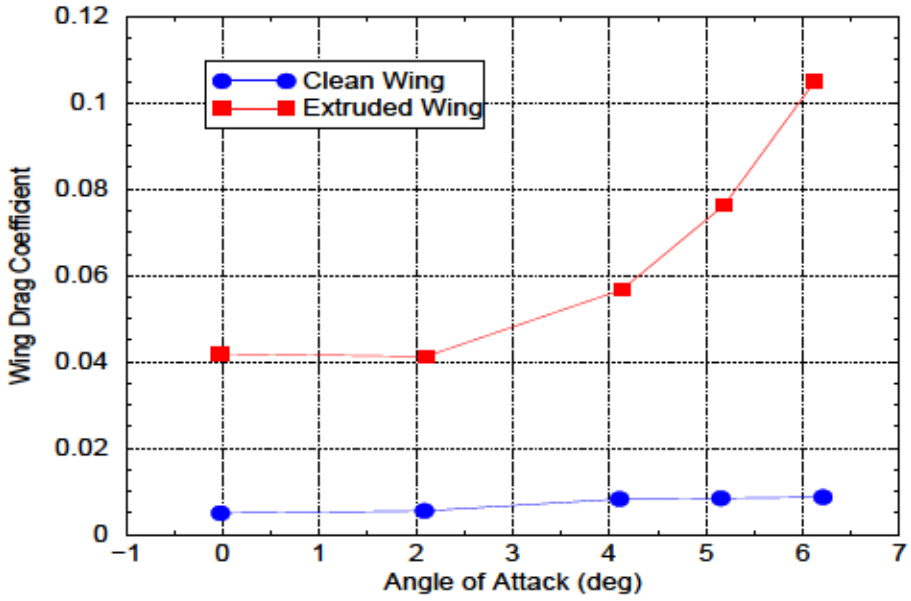

(b) Experimental drag coefficients

Figure 5.1: Comparison of experimental lift and drag coefficients for aircraft wing with GLC 305 airfoil section: with and without ice accretion (M=0.12 and Re=3.5x10^6) [5]

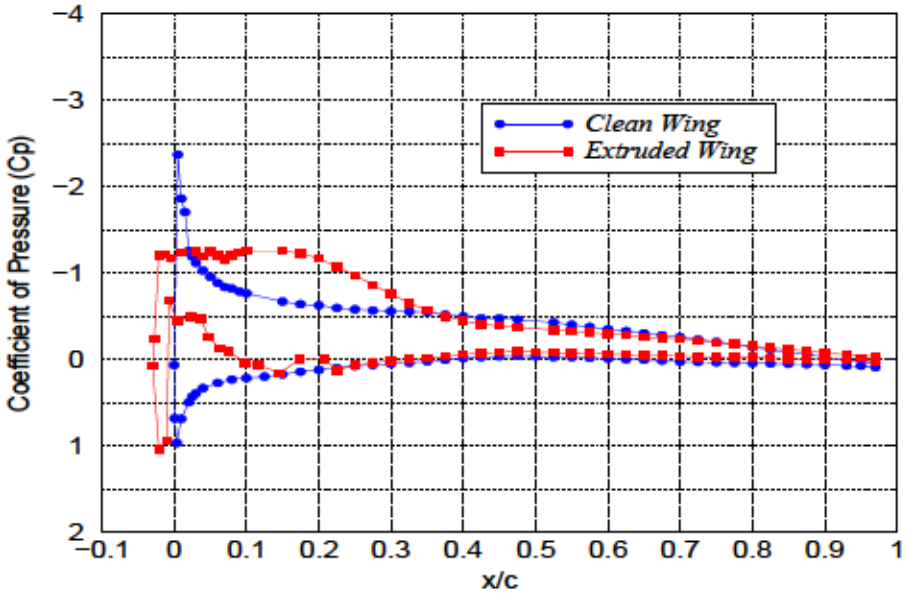

(a) =4°

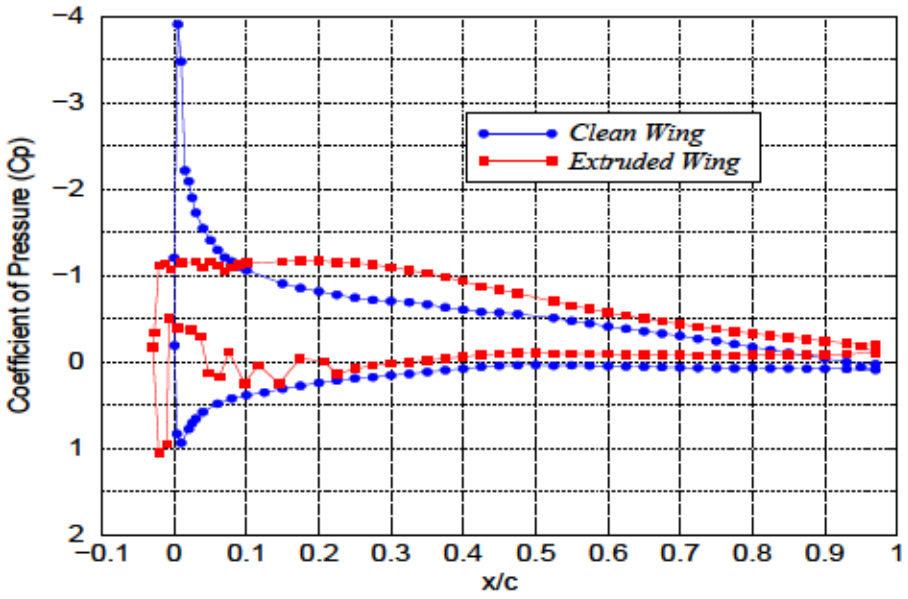

(b) =6°

Figure 5.2: Comparison of experimental pressure coefficients for aircraft wing with GLC 305 airfoil section: with and without ice accretion (M=0.12 and Re=3.5x10^6) [5]

(a) =4°

(b) =6°

Figure 5.3: Experimental time-averaged streamwise velocity plots for the extruded wing at angles of attack of 4° and 6° (M=0.12 and Re=3.5x10^6) [6]

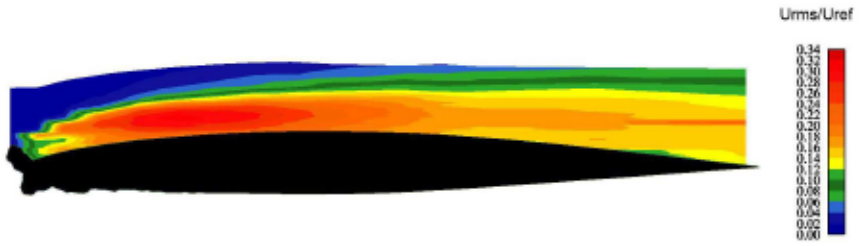

(a) =4°

(b) =6°

Figure 5.4: Experimental RMS of the fluctuations in the streamwise velocity component for the extruded 944-glaze-ice shape at angles of attack of 4° and 6° (M=0.12 and Re=3.5x10^6) [6]

5.1.2 Simulations

The computational approach adopted in this e ort was influenced by inferences drawn from the RANS and DES computations carried out by Mogili [20] and Mogili *et al.* [21]. The choice of mesh, time step size, and other factors considered during the RANS and hybrid RANS/LES computations were based on these prior e orts. The mesh used for the RANS and hybrid RANS/LES simulations of the extruded wing problem is the same as the "refined DES mesh" used by Mogili [20] and Mogili *et al.* [21] and shown in Figure 4.6. All computations for the extruded wing problem were performed for a Mach number of M=0.12 and a Reynolds number of Re=3.5x10^6.

It should be noted that the RANS and hybrid RANS/LES computations were carried out only at the "near stall" angles of attack of 4° and 6°. The RANS solutions for the extruded wing case were computed using an impulsive start and were continued until the normal force reached an approximate steady state. RANS solutions reported here were computed using first-order, implicit local time stepping and have formal second-order spatial accuracy. One Newton iteration, consisting of five Gauss-Seidel iterations, was employed per time step for RANS simulations. All hybrid RANS/LES solutions presented in this e ort were started from their respective converged RANS solutions. During the hybrid RANS-LES simulations, three Newton iterations, each consisting of ten Gauss-Seidel iterations, were employed per time step. The hybrid RANS-LES simulations were performed using second-order temporal accuracy. The computational results obtained by Mogili [20] and Mogili *et al.* [21] will be called as "AVUS results" hereafter for the sake of convenience. Results obtained in the current e ort will be called "CHEM results" with additional tags used as necessary.

5.1.3 RANS Simulations

The RANS results computed using CHEM are compared with experimental data [5, 6] as well as the computational results of Mogili [20] and Mogili *et al.* [21] computed using AVUS. The RANS solutions required 1 hour and 21 minutes per 100 iterations when run on 64 processors of the Maverick cluster [58]. About 21,000 iterations were performed for the 4° case and about 26,000 iterations were performed for the 6° case.

Figure 5.5 shows the convergence history for the RANS computations on the extruded wing at an angle of attack of 4°. The y-component of the total force on the wing is plotted against iteration count and the figure shows that it has reached an asymptotic value. This convergence history is representative of the computations for the other RANS simulations performed using CHEM.

Figure 5.6 shows comparisons of the wing lift and drag coefficients computed in the present e ort with AVUS RANS results and also with experimental data [5, 6]. Figure 5.6(a) shows that although the CHEM result is slightly higher, both CHEM and AVUS underpredict the lift coefficient when compared with experimental data at 4° and 6° angles of attack. A premature break in the predicted lift curve slope characteristic of the "near stall" behavior of the wing is seen in the AVUS RANS results suggesting an overestimation of the flow separation. Whether CHEM simulations imitate this phenomena cannot be gauged because simulations were carried out only for the two "near stall" angles of attack. Figure 5.6(b) shows the drag coefficients computed by CHEM compared with the AVUS results and experimental data. Although the drag coefficients computed using both AVUS and CHEM were underpredicted, AVUS results show better agreement with experimental data indicating the e ect of the turbulence model used. This result

is in accordance with the work of Chung *et al.* who compared results computed using the Spalart-Allmaras model with results computed using the SST turbulence model [41].

Figures 5.7 and 5.8 show comparisons of the predicted midspan pressure coefficients computed by CHEM RANS simulations with experimental data as well as with AVUS results for the 4° and 6° cases. The spanwise variation of pressure along the wing surface is minimal.

The upper surface pressure distribution does not compare well with experimental data. The recompression region is shifted closer to the leading edge in both CHEM and AVUS results. At 4° angle of attack, CHEM RANS results show the upper surface recompression shifted closer to the leading edge when compared to AVUS RANS results. At 6° angle of attack, CHEM RANS results compare relatively well with the experimental data in the region starting from the leading edge until $x/c \approx 0.1$ after which there is an increase in pressure and then the trend in C_P matches the AVUS RANS results along the remainder of the chord length.

Although the lower surface pressure distribution for both angles of attack is qualitatively similar when compared with experimental data, the pressure distribution predicted by CHEM conforms better to the general trend shown in the experimental data than does the AVUS prediction. The AVUS results for the lower surface in the region near the ice shape show characteristics that are similar to the upper surface pressure distribution. The lower surface pressure plateau suggests that the flow separates o the lower ice horn and fails to reattach. The CHEM results, which respond to the lower surface ice shape in a manner similar to the experimental data, suggest that the flow reattaches.

Figure 5.9 shows comparisons of the streamwise velocity component from the RANS simulations with experimental data and AVUS results for a 4° angle of

attack. The results show that the reattachment location is slightly underestimated when compared with AVUS RANS results and with experimental data. The reattachment location predicted by AVUS is closer to the experimental position when compared to CHEM results. The extent of the recirculation region (the three shades of blue) is smaller and shifted closer to the leading edge when compared to both AVUS and experimental data.

Figure 5.10 shows comparisons of the streamwise velocity component from the RANS simulations with experimental data and AVUS results for a 6° angle of attack. The results show that the extent of the upper surface bubble region predicted by CHEM, although slightly underpredicted, is in much better agreement with experimental data when compared to AVUS results. CHEM and AVUS results show streamwise velocities in the region near the trailing edge that are generally lower than those seen in the experimental data. Further, on the lower surface, the boundary layer downstream of the horn is observably thinner in the CHEM results than in the AVUS results, which supports the previous conclusion regarding flow reattachment in the CHEM results and the lack thereof in the AVUS results. The apparent dissimilarity in results predicted by CHEM and AVUS may be due to either the use of the SST turbulence model in CHEM and the Spalart-Allmaras model in AVUS or the e ects of preconditioning in the CHEM results.

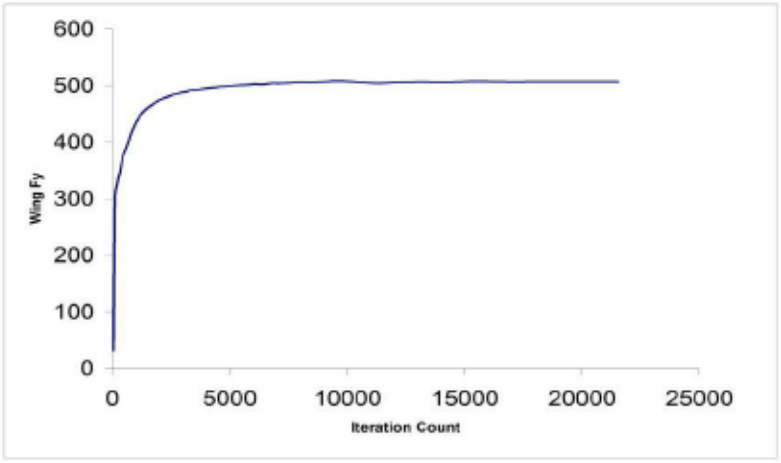

Figure 5.5: Convergence of RANS computations for the extruded 944-glaze-ice shape at 4° angle of attack)

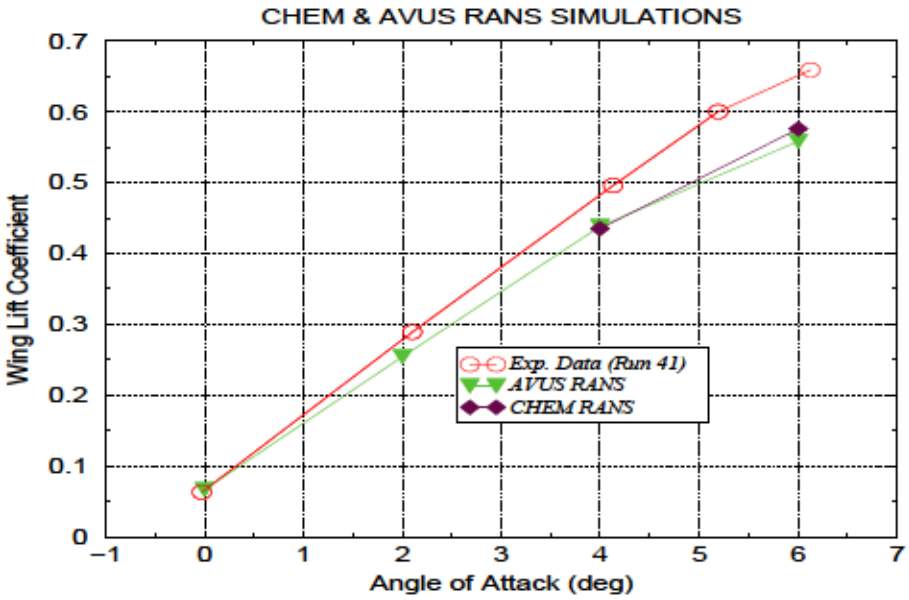

(a) Comparison of lift coefficients with experimental and AVUS data

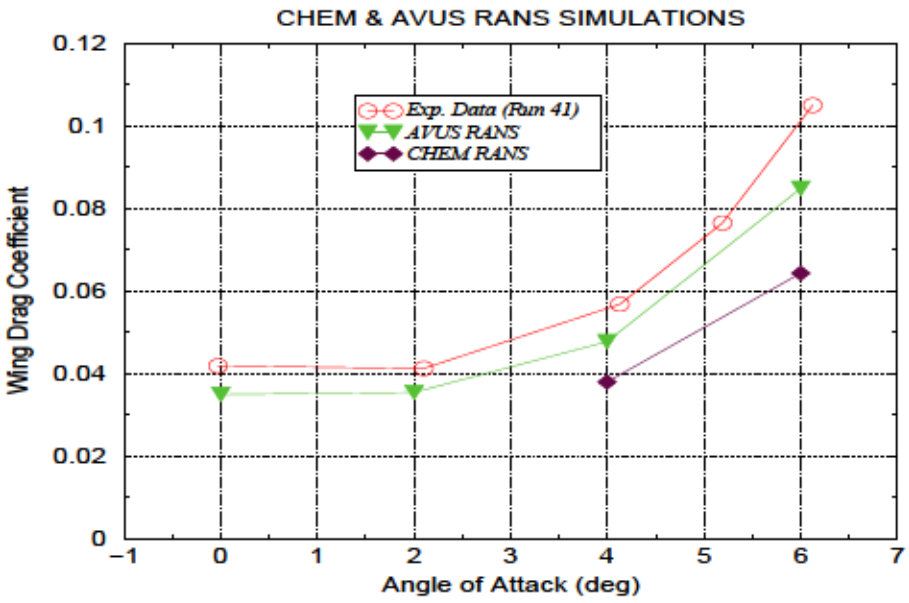

(b) Comparison of drag coefficients with experimental and AVUS data

Figure 5.6: Comparison of predicted midspan wing lift and drag coefficients with experimental data and AVUS results for the extruded 944-glaze-ice shape

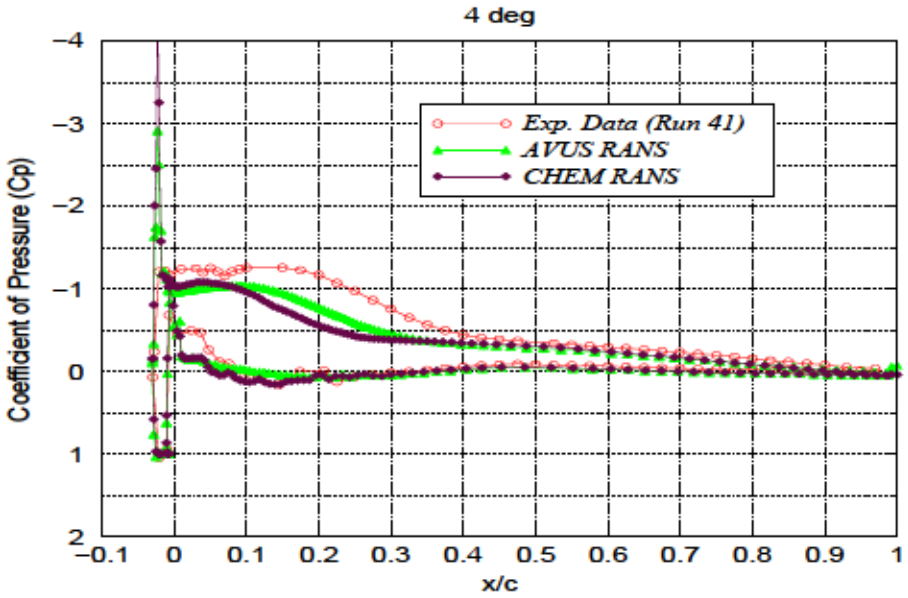

Figure 5.7: Comparison of predicted (RANS) pressure coefficients (midspan) with experimental data and AVUS results for the extruded 944-glaze-ice shape at 4° angle of attack

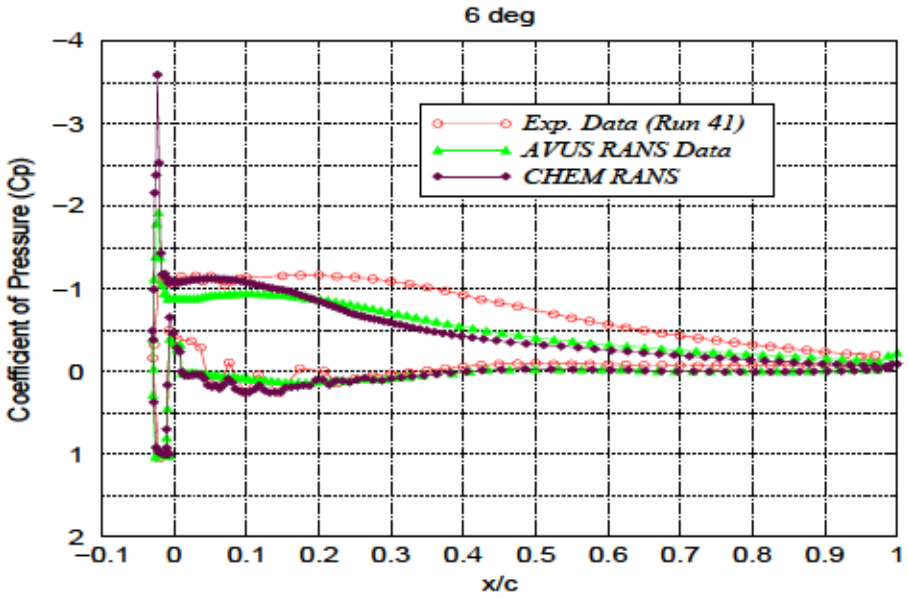

Figure 5.8: Comparison of predicted (RANS) pressure coefficients (midspan) with experimental data and AVUS results for the extruded 944-glaze-ice shape at 6° angle of attack

(a) AVUS RANS streamwise velocity contours [20, 21]

(b) CHEM RANS streamwise velocity contours

(c) Experimental hot-split-film data [6]

Figure 5.9: Comparison of predicted (RANS) streamwise velocity contours (midspan) with experimental data and AVUS results for the extruded 944-glaze-ice shape at 4° angle of attack

(a) AVUS RANS streamwise velocity contours [20, 21]

(b) CHEM RANS streamwise velocity contours

(c) Experimental hot-split-film data [6]

Figure 5.10: Comparison of predicted (RANS) streamwise velocity contours (midspan) with experimental data and AVUS results for the extruded 944-glaze-ice shape at 6° angle of attack

5.1.4 Hybrid RANS/LES Simulations

In this section, hybrid RANS/LES results computed using CHEM are compared with AVUS DES results [20, 21] and experimental data [5, 6]. A time step of Δt=0.075ms was used in the computations. The time taken for the hybrid RANS/LES solutions using CHEM was 4 hours and 58 minutes for every 100 time steps when run on 64 processors on the Maverick cluster.

Figure 5.11 shows comparisons of the time-averaged lift and drag coefficients obtained from the RANS and hybrid RANS/LES computations using CHEM with RANS and DES results from AVUS and with experimental data. Figure 5.11(a) shows that the lift coefficients predicted by hybrid RANS/LES simulations using CHEM are closer to the experimental data than the RANS results from both AVUS and CHEM at 4° and 6° angles of attack. The lift coefficient predicted by the CHEM hybrid RANS/LES simulations at 4° angle of attack agrees closely with the experimental data and is seen to be an improvement over the DES results of AVUS. At 6° angle of attack, the lift coefficient predicted by the hybrid RANS/LES simulations using CHEM is slightly overpredicted when compared with experimental data while the DES result of AVUS predicts a lift coefficient close to the experimental value.

Other quantities compared include the time-averaged streamwise component of velocity at midspan, the mean midspan pressure distribution, the RMS of the fluctuations in the streamwise velocity component and, for the 6° case, the time-averaged vertical velocity magnitude velocity component. These results and appropriate comparisons will be discussed in the following two sections that consider the 4° and 6° angle of attack cases separately.

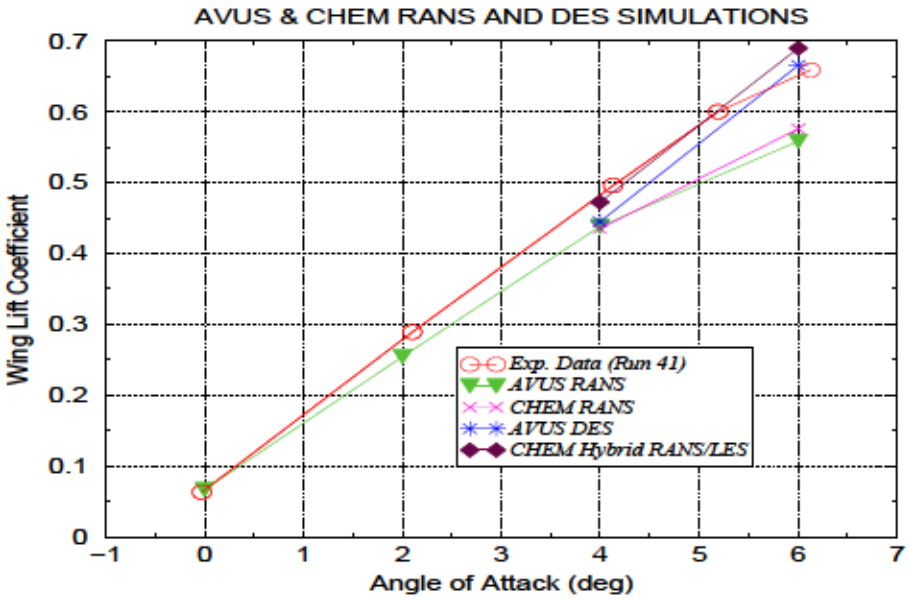

(a) Comparison of lift coefficients with experimental and AVUS data

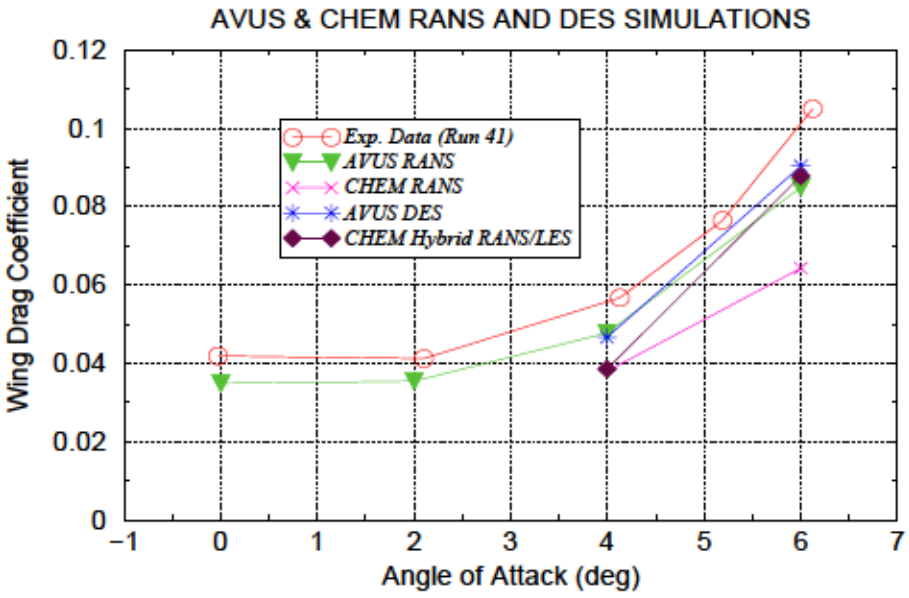

(b) Comparison of drag coefficients with experimental and AVUS data

Figure 5.11: Comparison of predicted midspan wing lift and drag coefficients with experimental data and AVUS results for the extruded 944-glaze-ice shape

5.1.4.1 Extruded wing at α=4°

In this section, CHEM hybrid RANS/LES results obtained for 4° angle of attack are compared with experimental data and with AVUS results. Figure 5.12 shows the history of the y-component of the total force on the wing for the hybrid RANS/LES computations at an angle of attack of 4°. A time step size one order of magnitude lower than the desired value was used to start the computation from the converged RANS solution. After about 16,000 time steps, the time step was increased to the desired value of Δt=0.075ms. This change was marked by an increase in fluctuations in F_y as can be seen in Figure 5.12. The simulation was continued for a period of time after the start of quasi-periodicity in the unsteadiness. Time averaging was performed over a period of 2050 time steps corresponding to a total time of 0.154 seconds.

Figure 5.13 shows comparisons of the predicted mean midspan pressure distribution computed using CHEM with AVUS DES results and with experimental data. The time-averaged AVUS DES results and CHEM hybrid RANS/LES results exhibit a relatively constant pressure region on the upper surface extending from the leading edge to $x/c \approx 0.21$ whereas, for the experimental data, pressure is seen to be constant from the leading edge to $x/c \approx 0.16$. This constant pressure region is indicative of the flow separating from the ice shape and forming a bubble aft of the ice shape. At the end of this constant pressure plateau, pressure increases as the flow reattaches. AVUS results show a slightly more abrupt increase in pressure at the end of the constant pressure region when compared to CHEM results and experimental data. It should be noted that the C_P value in this constant pressure region is higher for both AVUS and CHEM when compared to experimental data. This discrepancy suggest that separation from the horn is delayed in the flow

simulations relative to the experimental data. One possible explanation is that the flow is assumed to be fully turbulent in the simulations while the physical flow on the upstream side of the horn is probably laminar due to the presence of a favorable pressure gradient. Since a turbulent boundary typically shows less response to an adverse pressure gradient than a laminar boundary, the laminar boundary layer separates earlier.

Although the pressure distribution on the lower surface is qualitatively similar to the experimental data along most of the chord length, there are quantitative di erences between AVUS results and CHEM results for the region extending from the leading edge to $x/c \approx 0.25$. While AVUS results show a relatively constant pressure distribution after a steep climb in pressure very close to the leading edge, the experimental data show that the steep climb in the pressure coefficient is broken by a small constant pressure plateau until $x/c \approx 0.04$. As in the RANS results, CHEM results show better agreement with experimental data after $x/c \approx 0.04$.

Figure 5.14 shows comparisons of CHEM hybrid RANS/LES results with AVUS results and experimental data for the time-averaged streamwise component of velocity at midspan. From Figure 5.14, it can be estimated that the mean flow is separated for about 40% of the chord as shown by the hybrid RANS/LES results of CHEM while experimental data shows that the mean flow is separated for about 30% of chord. Corresponding AVUS DES results show a reattachment at approximately 40% of the chord. Although the streamwise velocities near the trailing edge predicted by both AVUS and CHEM are seen to be generally lower than the experimental data, CHEM results show slightly higher velocities relative to AVUS results as evidenced by the narrower wake in the CHEM result.

Figure 5.15 shows comparisons of the RMS of the fluctuations in streamwise velocity component predicted by hybrid RANS/LES solution of CHEM with AVUS

DES solution and experimental data. The RMS of the fluctuations in streamwise velocity for all the cases was calculated as the root-mean-square of the fluctuating streamwise velocity normalized by the streamwise velocity. Although the fields computed by both CHEM and AVUS are qualitatively similar when compared to experimental data, the region where the RMS of the fluctuations in the streamwise velocity is larger is shifted further aft of the ice shape for both CHEM and AVUS results. This shift is more apparent in the AVUS results than for the CHEM results. The region where the RMS of the fluctuations in the streamwise velocity is larger is seen to be thicker and extends further downstream of the horn for the AVUS DES results than for the hybrid RANS/LES results of CHEM.

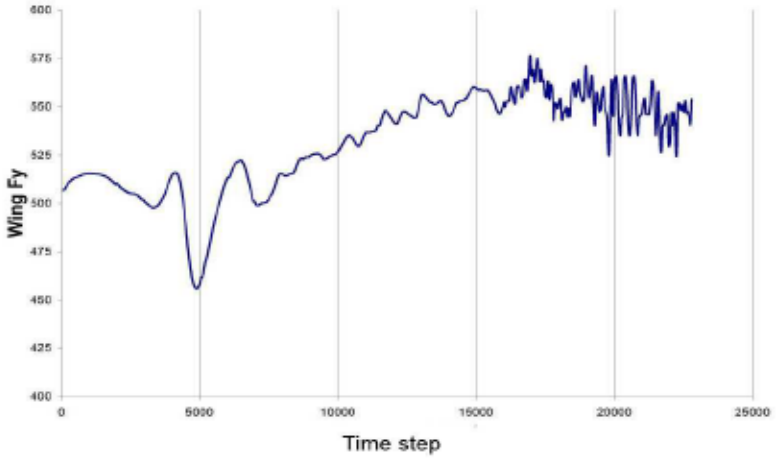

Figure 5.12: F_y history for Hybrid RANS/LES computations for the extruded 944-glaze-ice shape at 4° angle of attack)

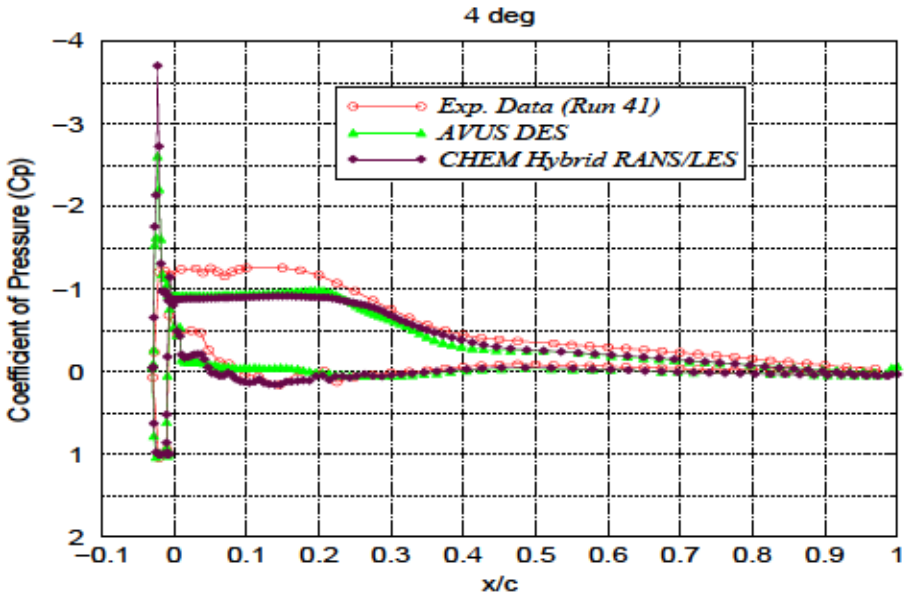

Figure 5.13: Comparison of predicted (Hybrid RANS/LES) pressure coefficients (midspan) with experimental data and AVUS results for the extruded 944-glaze-ice shape

(a) AVUS DES streamwise velocity contours [20, 21]

(b) CHEM Hybrid RANS/LES streamwise velocity contours

(c) Experimental hot-split-film data [6]

Figure 5.14: Comparison of predicted (Hybrid RANS/LES) streamwise velocity contours (midspan) with experimental data and AVUS results for the extruded 944-glaze-ice shape at 4° angle of attack

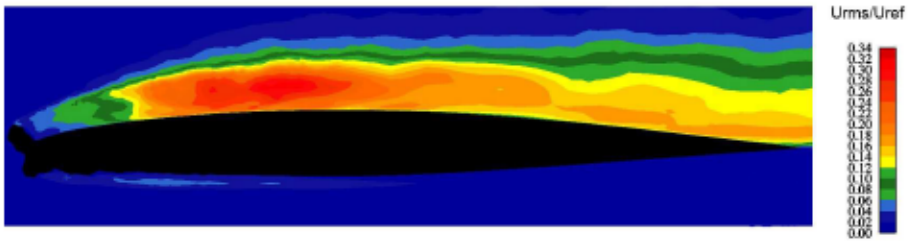

(a) AVUS DES results [20, 21]

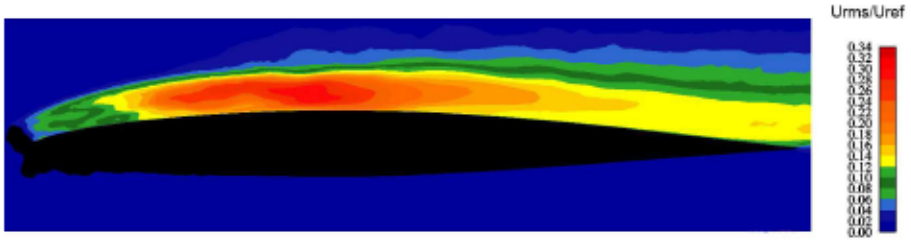

(b) CHEM Hybrid RANS/LES results

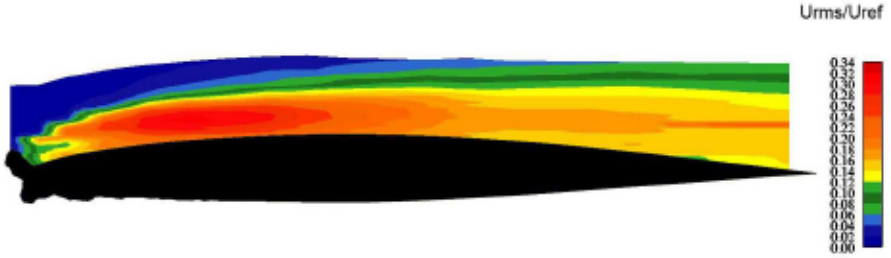

(c) Experimental hot-split-film data [6]

Figure 5.15: Comparison of RMS of the fluctuations in the streamwise velocity component for the extruded 944-glaze-ice shape at 4° angle of attack

5.1.4.2 Extruded Wing at α=6°

In this section, hybrid RANS/LES results computed using CHEM for an angle of attack of 6° are compared with experimental data and with AVUS results. Figure 5.16 shows the history of the y-component of the total force on the wing. As with the 4° case, a time step one order of magnitude lower than the desired value was used to start the computation from the converged RANS solution. Since there were no indications (from this plot) of any quasi periodicity in the unsteadiness, a C_L Vs C_D plot was also made to assess the flow behavior. In the C_L vs C_D plot shown in Figure 5.17, the clustering of points in the upper half of the plot depicts higher frequency fluctuations. An apparent repetition of a lower frequency oscillation was taken to be a sign of quasi-periodicity within the unsteadiness. Time averaging was performed over a period of 7700 time steps starting at a time step of 19,200 corresponding to a total time of 0.578 seconds.

Figure 5.18 shows comparisons of the predicted mean midspan pressure distribution with the AVUS DES results and with experimental data. The upper surface pressure distribution computed using CHEM is quite similar to the AVUS DES results and neither compares well with the experimental data. The time-averaged AVUS DES and CHEM hybrid RANS/LES results indicate a relatively constant pressure region on the upper surface extending from the leading edge to $x/c \approx 0.3$ whereas, for the experimental data, pressure is seen to be constant from the leading edge to $x/c \approx 0.2$. As noted previously, the discrepancy in the plateau pressure is likely due to the assumption that the flow is fully turbulent. Di erences in the pressure distributions on the lower surface can be seen in the region extending from the leading edge to $x/c \approx 0.25$. Again, CHEM results follow the general fluctuations of the experimental data whereas AVUS results

show a relatively constant pressure distribution throughout most of the region, which is indicative of a region of separated flow. For the remainder of the chord, the lower surface pressure distribution predicted by CHEM hybrid RANS/LES is qualitatively similar to AVUS DES results and the experimental data. An upward shift in the pressure distribution in the experimental data is consistent with the shift seen in Figure 5.2(b).

Figure 5.19 shows comparisons of CHEM hybrid RANS/LES results with AVUS DES results and experimental data for the time-averaged streamwise component of velocity at midspan. The CHEM results are similar to the AVUS results. The extent of the separation bubble is overpredicted in both cases when compared to experimental data. On closer examination it can be seen that the reattachment location predicted by AVUS is near the trailing edge, whereas CHEM predicts a reattachment location slightly upstream.

Comparisons of the RMS of the fluctuations in the streamwise velocity are shown in Figure 5.20. Although the fields predicted by CHEM hybrid RANS/LES results are qualitatively similar to AVUS DES results as well as with experimental data, the region where the RMS of the fluctuations in the streamwise velocity is maximum is shifted downstream for both CHEM and AVUS results. This apparent shift is seen to be slightly more prominent in the AVUS DES results than in the CHEM hybrid RANS/LES results. This phenomenon can be inferred by the relatively higher intensities of the RMS of the fluctuations predicted by CHEM in the region close to the ice shape when compared to AVUS results.

Figure 5.21 shows comparisons of CHEM hybrid RANS/LES results with AVUS DES results and experimental data for the time-averaged value of the vertical velocity magnitude at midspan. The experimental data shows two regions of high velocity magnitude in the region downstream of the horn. AVUS DES results also

show two regions of higher velocity. However, the average velocity magnitude is significantly lower and the locations are shifted relative to the experimenal data. CHEM hybrid RANS/LES results, although similar to the AVUS DES results in terms of the velocity magnitude do not capture the two high magnitude regions seen in the AVUS results and experimental data. Only a single region near the trailing edge is observed. The higher magnitudes observed in the experimental data suggest a more active "roll up" than is present in the CHEM and AVUS simulations. Therefore, the shift of the region of maximum fluctuation intensity shown in Figure 5.20 is likely caused by "flapping" of the shear layer rather than shear layer "roll up".

A Strouhal number based on the horn projected height and the freestream velocity was calculated. A visual identification based on the major vortex shedding phenomena as inferred from swirl images plotted after every 50 time steps was used to calculate the vortex shedding frequency. The Strouhal number was estimated to be about 0.019 and is close to the experimental value of about 0.015 for a NACA 0012 airfoil with a glaze ice accretion obtained by Zaman *et al.* [59].

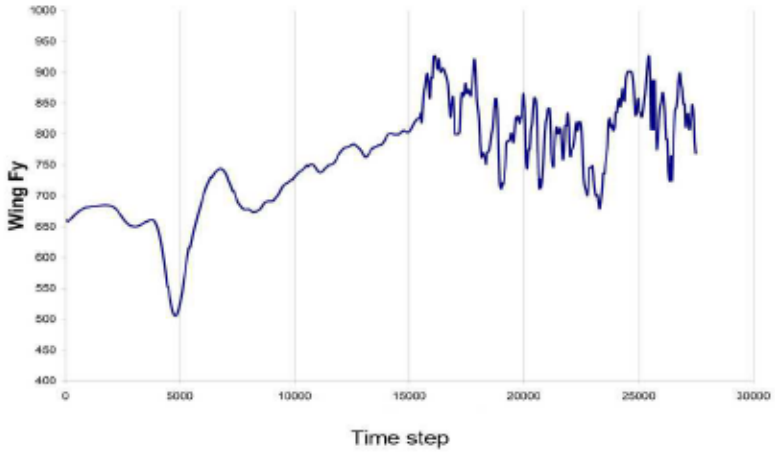

Figure 5.16: F_y history for hybrid RANS/LES computations for the extruded 944-glaze-ice shape at 6° angle of attack)

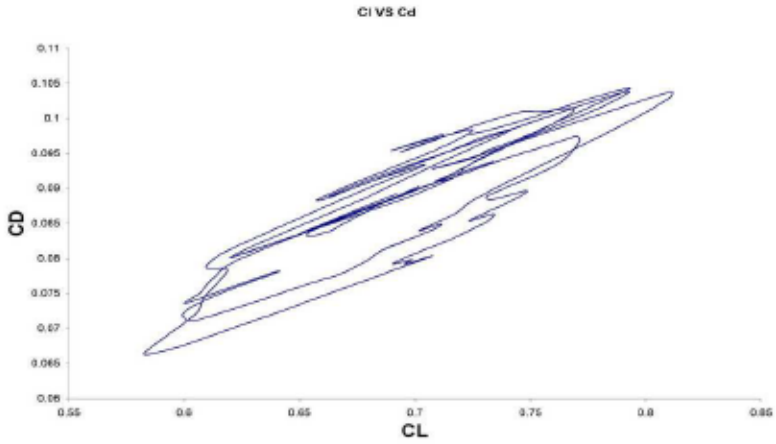

Figure 5.17: C_L vs C_D plot for the extruded 944-glaze-ice shape at 6° angle of attack)

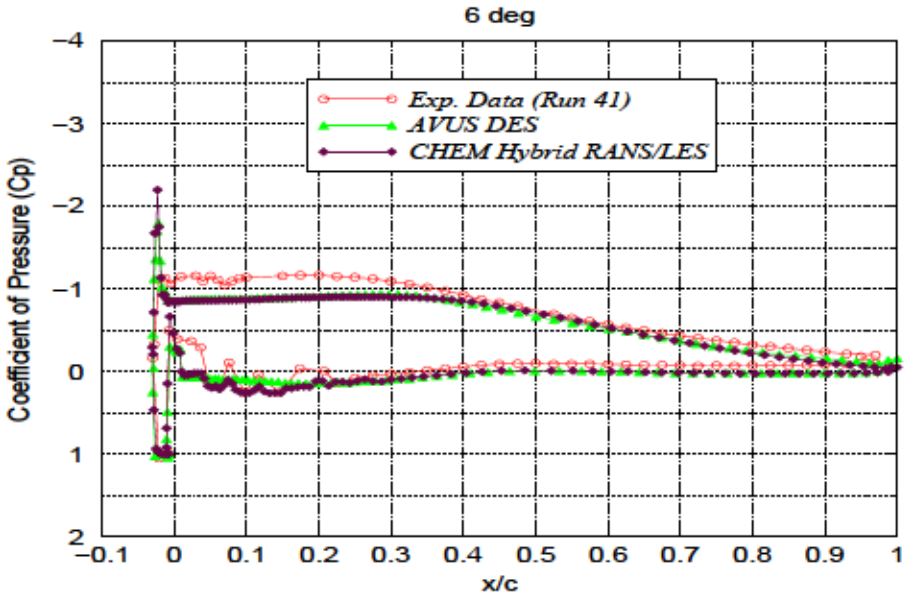

Figure 5.18: Comparison of predicted (Hybrid RANS/LES) pressure coefficients (midspan) with experimental data and AVUS results for the extruded 944-glaze-ice shape

(a) AVUS DES streamwise velocity contours [20, 21]

(b) CHEM Hybrid RANS/LES streamwise velocity contours

(c) Experimental hot-split-film data [6]

Figure 5.19: Comparison of predicted (Hybrid RANS/LES) streamwise velocity contours (midspan) with experimental data and AVUS results for the extruded 944-glaze-ice shape at 6° angle of attack

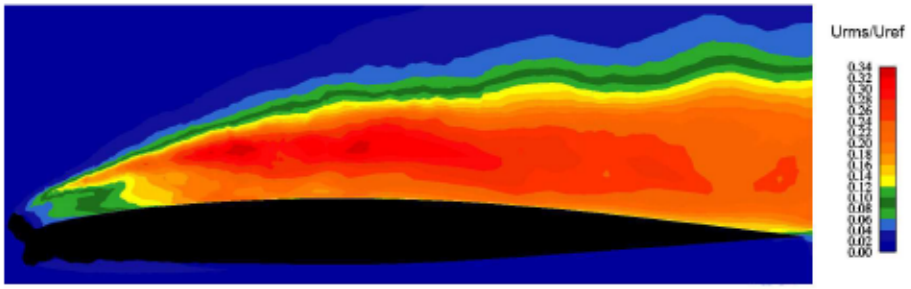

(a) AVUS DES results [20, 21]

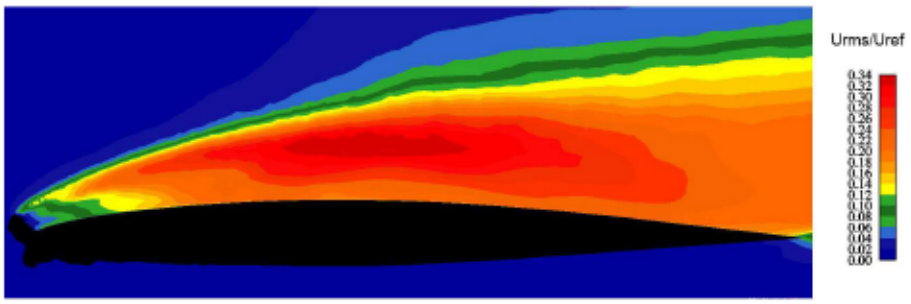

(b) CHEM Hybrid RANS/LES results

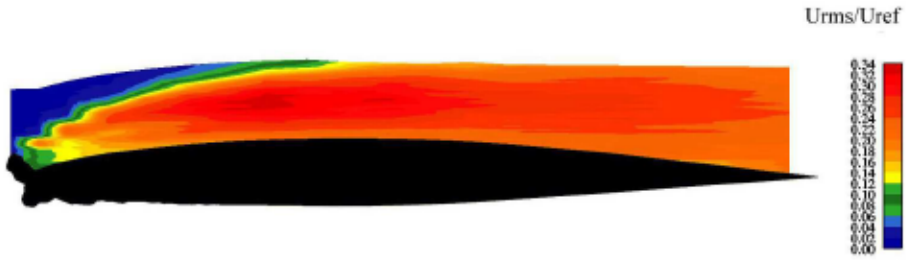

(c) Experimental hot-split-film data [6]

Figure 5.20: Comparison of RMS of the fluctuations in the streamwise velocity component for the extruded 944-glaze-ice shape at 6° angle of attack

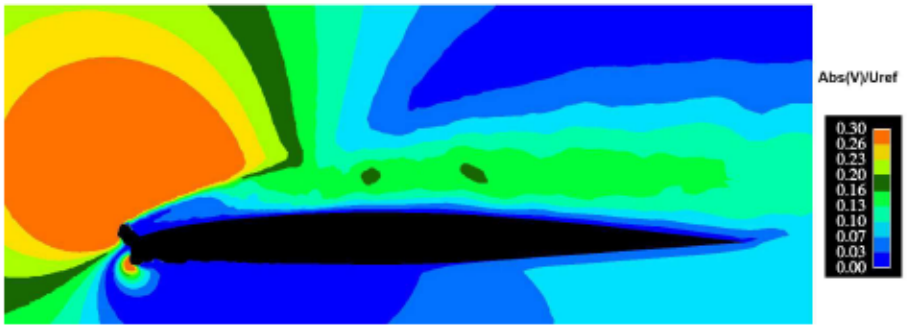

(a) AVUS DES vertical velocity contours [20, 21]

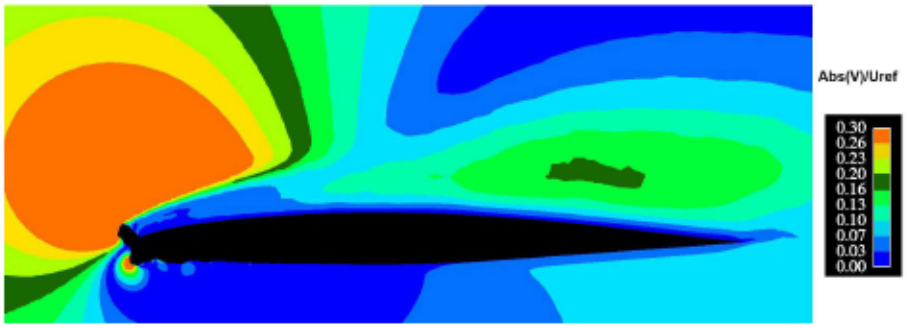

(b) CHEM Hybrid RANS/LES vertical velocity contours

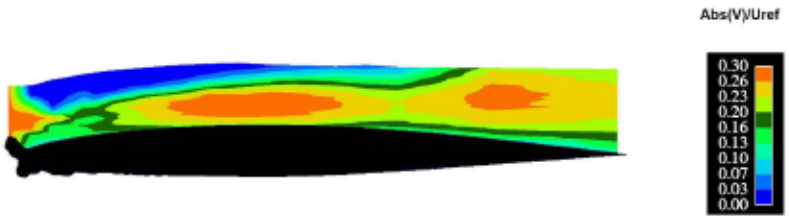

(c) Experimental hot-split-film data [6]

Figure 5.21: Comparison of predicted (Hybrid RANS/LES) vertical velocity contours (midspan) with experimental data and AVUS results for the extruded 944-glaze-ice shape at 6° angle of attack

5.2 Swept Wing Configuration

5.2.1 Experimental Details

Bragg *et al.* [7] obtained Laser Doppler Velocimeter (LDV) measurements to study the e ects of a simulated glaze-ice accretion on the flow field about a three-dimensional wing for a zero sweep configuration and a 30° sweep configuration. It should be noted that all discussion in this section pertains to the swept wing configuration. The model, a NACA 0012 airfoil section on a rectangular, untwisted planform, was mounted from the sidewall of the University of Illinois at Urbana-Champaign subsonic wind tunnel. The NACA 0012 airfoil section was defined in a plane perpendicular to the leading edge. A simulated ice-accretion, as measured on a NACA 0012 airfoil in the NASA Icing Research Tunnel [50], was added to the leading edge. The model had a span of 35.18 inches and the chord in the streamwise direction was 17.32 inches. The iced swept wing geometry and the wing profile can be seen in Figure 1.7. The flow velocity was measured using a four-beam two-color fiber optic LDV. The measurements were taken at a Reynolds number of Re=1.0x10^6 at 8° angle of attack. Measurements were obtained for the three velocity components at four spanwise locations of y/b=0.40, y/b=0.55, y/b=0.70 and y/b=0.85.

Bragg *et al.* observed that the flow field is characterized by a leading edge vortex formed due to flow separation o the ice horn. At 8° angle of attack, the vortex grows in diameter and moves along the span before it reaches the wing tip. The measurements at y/b=0.40 and y/b=0.55 showed the vortex growing in size with its axis almost parallel to the leading edge.

Figure 5.22 shows the time-averaged streamwise velocity component at four spanwise locations. A high velocity region is visible above the separation bubble

(with U/U_{ref} above 1.4) at y/b=0.40 and y/b=0.55 starting behind the ice shape and proceeding chordwise until $x/c \approx 0.4$. Growth in the chordwise extent of the separation bubble can be seen at y/b=0.55 when compared to the plane at y/b=0.40. At y/b=0.40, the reattachment location is at $x/c \approx 0.2$ whereas, at y/b=0.55, it can be seen to have shifted downstream to $x/c \approx 0.5$. Planes at spanwise locations of y/b=0.70 and y/b=0.85 approximately bound the region where the vortex moves chordwise while traversing the span toward the wing tip. The magnitude of the reversed flow also grows as the wing tip is approached. The streamwise velocity component at y/b=0.70 and y/b=0.85 shows that there is a significant increase in the extent of the separation bubble when compared to the measurements at y/b=0.40 and y/b=0.55. It should be noted that although the streamwise velocity plot at y/b=0.85 is qualitatively similar to that at y/b=0.70, there are some di erences in the general flow behavior at y/b=0.85 due to the interaction of the wing tip vortex with the leading edge vortex. The flow near the wing tip is significantly influenced by the tip vortex.

Figure 5.23 shows the RMS of the fluctuations in the streamwise velocity component for the swept wing configuration at four spanwise locations. The experimental data shows that the chordwise extent of the region of larger values of the RMS increases moving along the span toward the wing tip. At y/b=0.85, a region of relatively high RMS values can be seen. This indicates that the flow at this spanwise location (close to the wing tip) is highly unsteady because of the interaction of the wing tip vortex with the leading edge vortex.

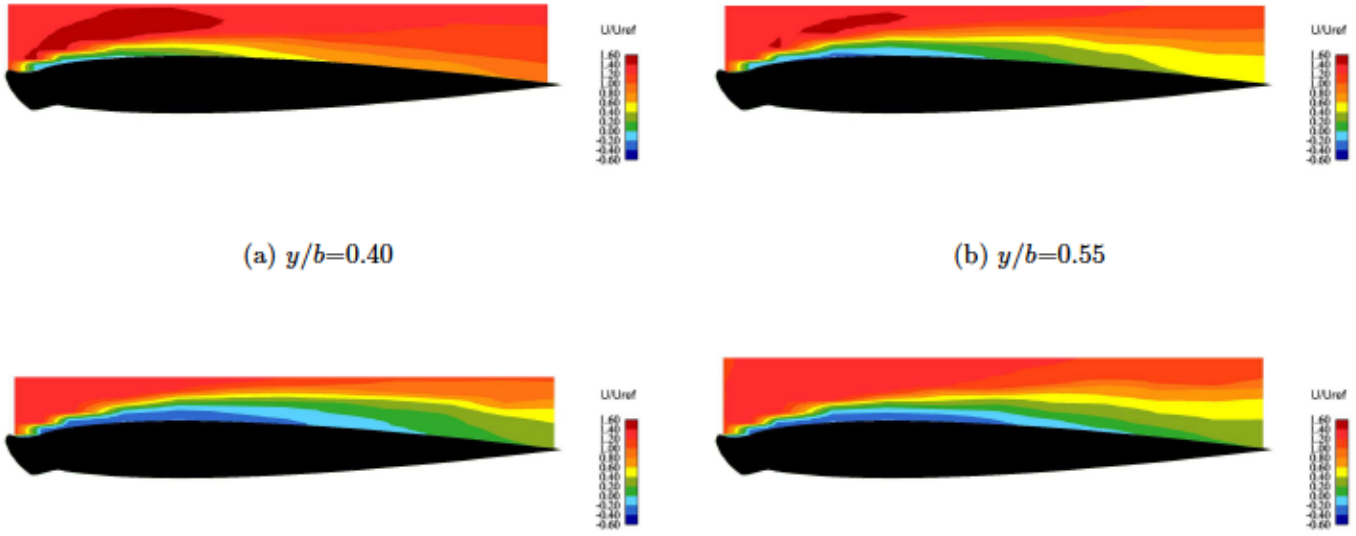

(a) y/b=0.40

(b) y/b=0.55

(c) y/b=0.70

(d) y/b=0.85

Figure 5.22: Experimental time-averaged streamwise velocity plots at four spanwise locations [7]

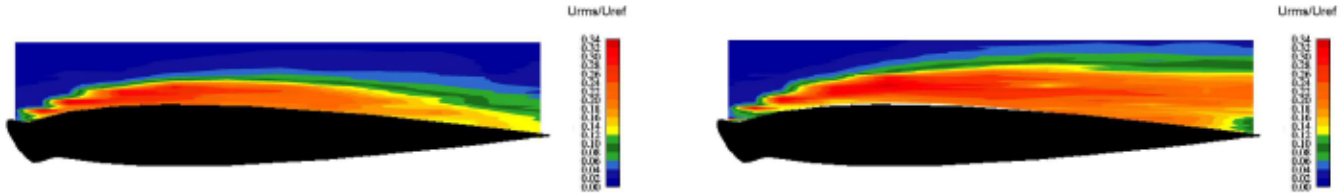

(a) y/b=0.40

(b) y/b=0.55

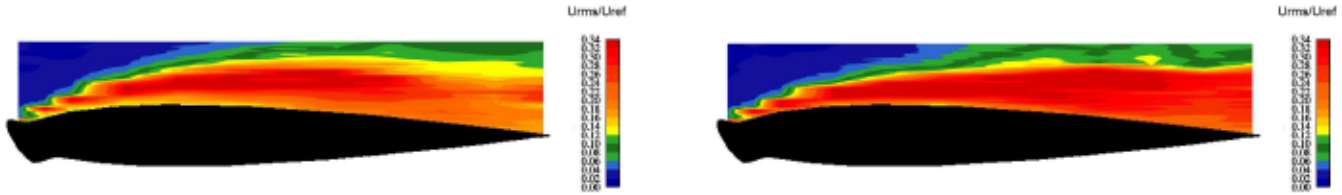

(c) y/b=0.70

(d) y/b=0.85

Figure 5.23: Experimental RMS of the fluctuations in the streamwise velocity component for the swept wing configuration at four spanwise locations [7]

5.2.2 Simulations

RANS and hybrid RANS/LES computations were carried out for a Mach number of M=0.105 at 8° angle of attack. The mesh used for this case is shown in Figure 4.6. A time step of Δt=0.05ms was used in the hybrid RANS/LES computations.

The RANS solutions were computed using an impulsive start and were run until the normal force reached an approximate steady state. One Newton iteration, consisting of five Gauss-Seidel iterations, was employed per time step for RANS simulations. The RANS solutions were then used as initial conditions for the hybrid RANS/LES simulation. The SST turbulence model [25] was again employed. During the hybrid RANS/LES simulations, three Newton iterations, each consisting of ten Gauss-Seidel iterations, were employed per time step.

5.2.3 RANS and Hybrid RANS/LES Simulations

In this section, results of the RANS and hybrid RANS/LES computations performed on the swept wing configuration using CHEM are presented and compared with the corresponding experimental data [7]. The RANS solutions required 1 hour and 14 minutes per 100 iterations when run on 64 processors of the Maverick cluster [58]. About 8,000 iterations were performed for convergence. The time taken for the hybrid RANS/LES solutions using CHEM was 2 hours and 34 minutes for every 100 time steps when run on 128 processors of the Maverick cluster.

Figure 5.24 shows the history of the y-component of the total force on the swept wing for the hybrid RANS/LES simulation. During the initial stages of the run, it is seen that the the value of the y-component of the total force converges to an

asymptotic value suggesting convergence to a steady state. This is attributed to the fact that the simulations were inadvertently carried out with first-order temporal accuracy. Hybrid RANS/LES simulations were then continued from the converged state using second-order temporal accuracy. Time averaging was performed over a period of 5050 time steps and a total interval of 0.2525seconds starting at a time step of 9450.

Figure 5.25 shows a comparison of the predicted hybrid RANS/LES mean pressure distribution with RANS results at four spanwise locations. There are significant qualitative di erences in the upper surface pressure distribution when comparing the RANS and hybrid RANS/LES results. The constant pressure plateau seen in the RANS results extends to $x/c \approx 0.08$ at each spanwise station. The constant pressure plateau seen in the hybrid RANS/LES results extends further chordwise than the RANS results (to $x/c \approx 0.4$) and also exhibits a higher pressure. Both RANS and hybrid RANS/LES results show that the plateau pressure increases while moving spanwise toward the wing tip. The lower surface pressure distribution predicted by RANS and hybrid RANS/LES is similar and matches well till near the trailing edge, where slightly lower values are seen for the RANS results. This general agreement in the lower surface pressure distribution is seen at all spanwise locations and indicated that the flow is mostly steady on the lower surface.

Figures 5.26 to 5.29 show comparisons of the time-averaged streamwise component of velocity with CHEM RANS results with the experimental data [7] at four spanwise locations. In general, the RANS and hybrid RANS/LES results overpredict the extent of the reversed flow region when compared to the experimental data. Both RANS and hybrid RANS/LES results fail to predict the high velocity region above and aft of the ice shape found in the experimental

data. The RANS results also fails to predict high magnitude reversed flow regions seen in the experimental data. Although hybrid RANS/LES do predict the high magnitude reversed flow regions, its extent is underpredicted. In general, both RANS and hybrid RANS/LES results also show a broad wake in which the velocities are underpredicted relative to the experimental data.

Figure 5.26 shows the time averaged streamwise component of velocity obtained from RANS and hybrid RANS/LES simulations at y/b=0.40 compared with the experimental data [7]. The high velocity region above and aft of the ice shape found in the experimental data is not observed in the CHEM results. The extent of the separation bubble is overpredicted by RANS and hybrid RANS/LES when compared to experimental data. While the RANS results predict a reattachment location at $x/c \approx 0.3$ and the hybrid RANS/LES results show a reattachment at x/c=0.45, the experimental measurements show reattachment at x/c=0.23. The RANS and hybrid RANS/LES results show a broad wake in which the velocities are underpredicted relative to the experimental data while the hybrid RANS/LES results show a broad lower magnitude region on the upper surface which narrows near the trailing edge.

Figure 5.27 shows the streamwise component of velocity obtained from RANS and hybrid RANS/LES simulations at y/b=0.55 compared with the experimental data [7]. Again the high velocity region is not observed in the CHEM results. While the RANS results predict a reattachment location at $x/c \approx 0.6$ and the hybrid RANS/LES results show a reattachment at x/c=0.8, the experimental measurements show reattachment at x/c=0.5. The region with higher magnitude reversed flow (dark blue region) is not observed in the CHEM results. The upper surface velocities near the trailing edge are again underpredicted by CHEM.

Figure 5.28 shows the streamwise component of velocity obtained from RANS and hybrid RANS/LES simulations at y/b=0.70 compared with the experimental data [7]. Here, although RANS results show that the extent of the separated region is slightly underpredicted when compared to the experimental data, the hybrid RANS/LES results show that the extent of the separated region is overpredicted. While the RANS results predict a reattachment location at $x/c \approx 0.65$ and the hybrid RANS/LES results show a reattachment at x/c=0.85, the experimental measurements show reattachment at x/c=0.70. RANS and hybrid RANS/LES results also do not show the large region of high-magnitude reversed flow.

Figure 5.29 shows the streamwise component of velocity computed by RANS and hybrid RANS/LES simulations at y/b=0.85 compared with the experimental data [7]. CHEM results overpredict the extent of the separated region when compared to experimental data. The reattachment location is seen to be similar to the experimental data but the upper surface velocities near the trailing edge were underpredicted by RANS and hybrid RANS/LES simulations and the region of lower velocity extends farther into the field than the experimental data. The large region of high-magnitude reversed flow is not predicted by RANS simulation, while hybrid RANS/LES simulation predicts a high-magnitude reversed flow region. Its location is shifted aft.

Figures 5.30 to 5.33 show comparisons of the RMS of the fluctuations in the streamwise velocity obtained from hybrid RANS/LES results with the experimental data [7] at the four spanwise locations. In general, it is seen that lower magnitudes of the fluctuations are observed in the region just aft of the ice shape in the hybrid RANS/LES simulation at all four spanwise locations. Hybrid RANS/LES results also show that the extent of the fluctuating region is larger and shifted upward when compared to corresponding experimental data.

Figure 5.30 shows the RMS of the fluctuations in the streamwise velocity obtained from hybrid RANS/LES results compared with experimental data at y/b=0.40. The fluctuating region is seen to extend further into the flow than that seen in the experimental data. CHEM hybrid RANS/LES results also show a large region of low fluctuation behind the ice shape (extending to x/c=0.3) not seen in the experimental data. The region of high magnitude fluctuation (shown in bright red) is shifted up in the hybrid RANS/LES results when compared to experimental data.

Figure 5.31 shows the RMS of the fluctuations in the streamwise velocity obtained from hybrid RANS/LES results compared with experimental data at y/b=0.55. The fluctuating region in the hybrid RANS/LES results is again seen to extend further into the flow than in the experimental data with the region of high magnitude fluctuation broader and extending further aft. The low-fluctuation region seen in the hybrid RANS/LES results again extends to x/c=0.3.

Figure 5.32 shows the RMS of the fluctuations in the streamwise velocity obtained from hybrid RANS/LES results compared with experimental data at y/b=0.70. Although the high magnitude fluctuation region is similar in extent when comparing the hybrid RANS/LES results to the experimental data, it is shifted downstream and upwards of the experimental data.

Figure 5.33 shows the RMS of the fluctuations in the streamwise velocity obtained from hybrid RANS/LES results compared with experimental data at y/b=0.85. Here again, the high magnitude fluctuation region seen in the hybrid RANS/LES results is shifted downstream and upwards of the experimental data.

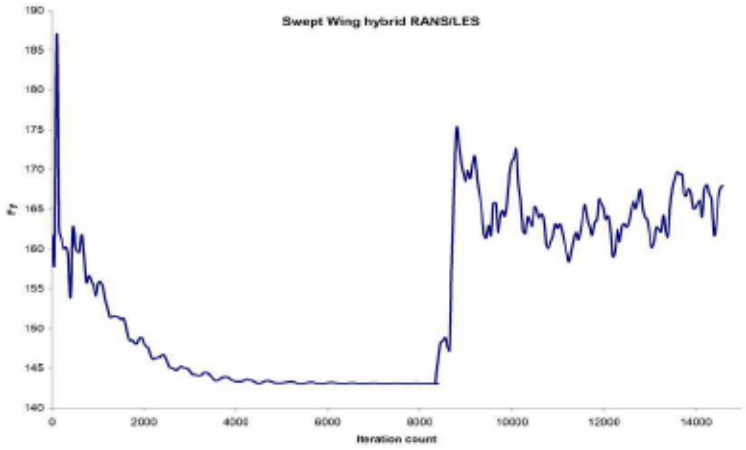

Figure 5.24: F_y history for Hybrid RANS/LES computations for the swept wing configuration

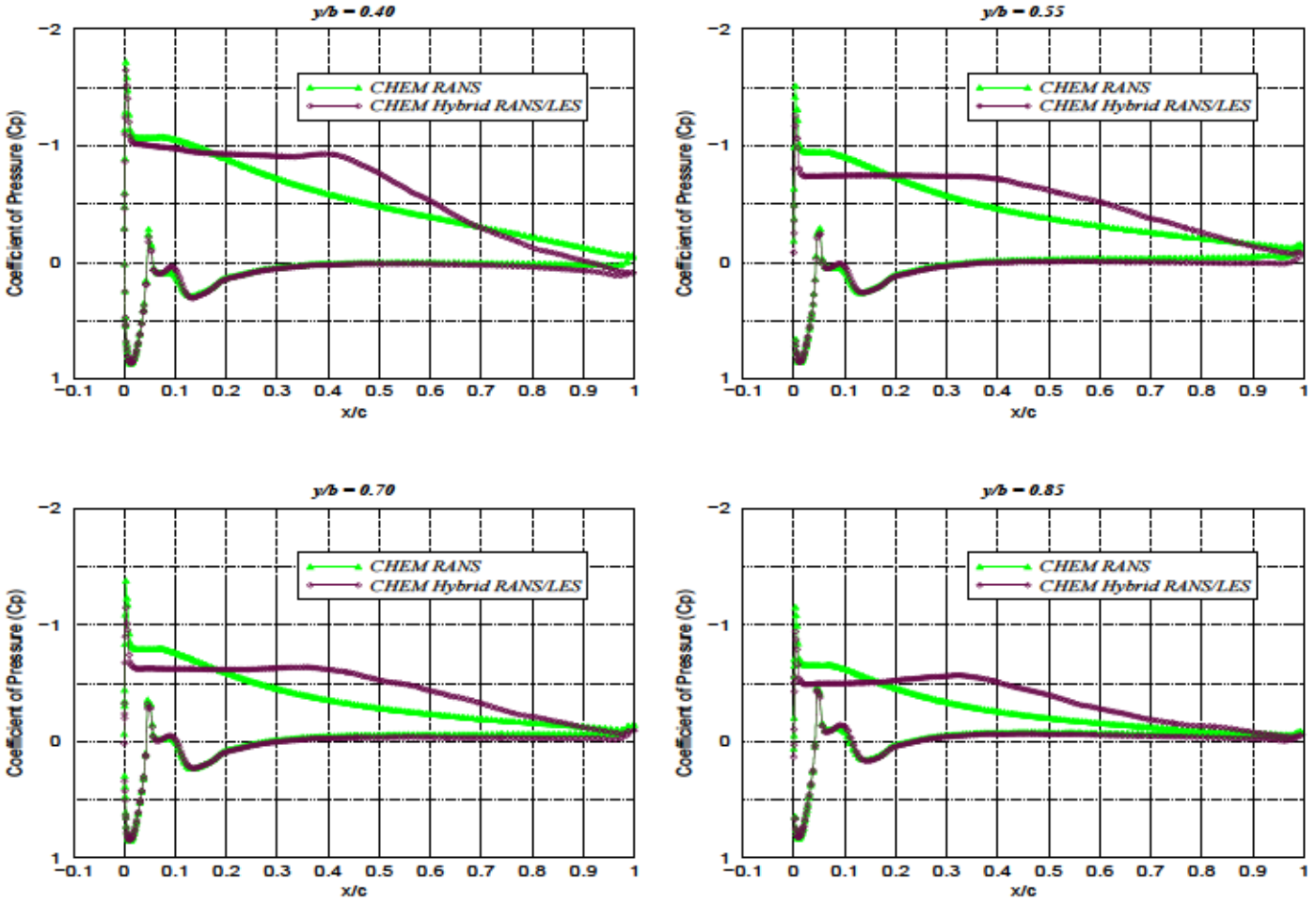

Figure 5.25: Comparison of predicted CHEM hybrid RANS/LES mean pressure distribution over the swept wing with CHEM RANS results at four spanwise locations

(a) CHEM RANS streamwise velocity contours

(b) CHEM Hybrid RANS/LES streamwise velocity contours

(c) Experimental data

Figure 5.26: Comparison of predicted (Hybrid RANS/LES) streamwise velocity contour at y/b=0.40 with CHEM RANS results and the experimental data for the swept wing configuration

(a) CHEM RANS streamwise velocity contours

(b) CHEM Hybrid RANS/LES streamwise velocity contours

(c) Experimental data

Figure 5.27: Comparison of predicted (Hybrid RANS/LES) streamwise velocity contour at y/b=0.55 with CHEM RANS results and the experimental data for the swept wing configuration

(a) CHEM RANS streamwise velocity contours

(b) CHEM Hybrid RANS/LES streamwise velocity contours

(c) Experimental data

Figure 5.28: Comparison of predicted (Hybrid RANS/LES) streamwise velocity contour at y/b=0.70 with CHEM RANS results and the experimental data for the swept wing configuration

(a) CHEM RANS streamwise velocity contours

(b) CHEM Hybrid RANS/LES streamwise velocity contours

(c) Experimental data

Figure 5.29: Comparison of predicted (Hybrid RANS/LES) streamwise velocity contour at y/b=0.85 with CHEM RANS results and the experimental data for the swept wing configuration

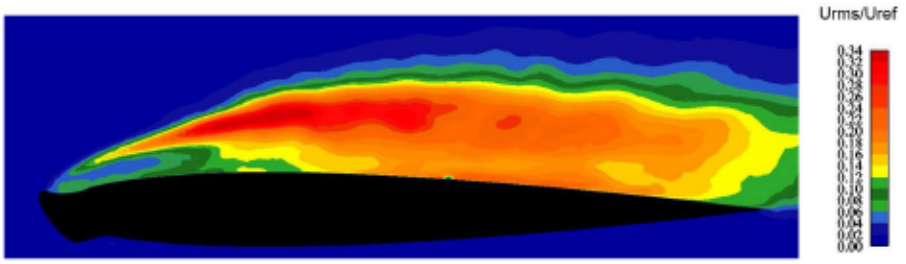

(a) CHEM hybrid RANS/LES

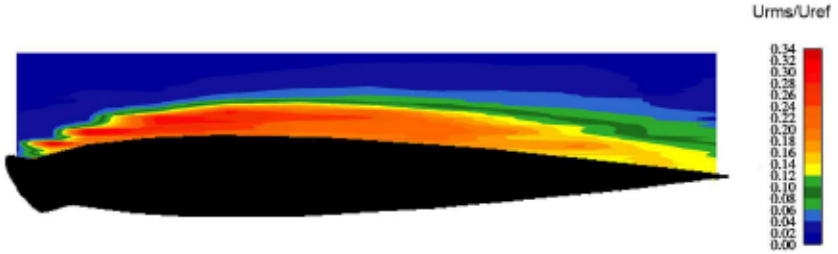

(b) Experimental data [7]

Figure 5.30: Comparison of RMS of the fluctuations in the streamwise velocity component for the swept wing configuration at y/b=0.40

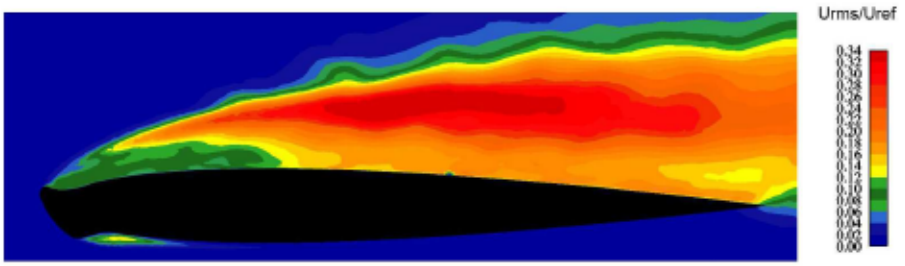

(a) CHEM hybrid RANS/LES

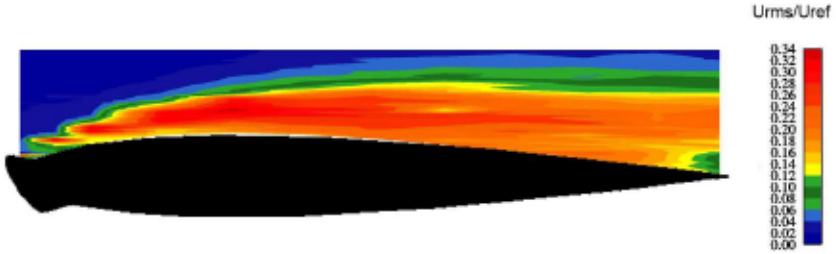

(b) Experimental data [7]

Figure 5.31: Comparison of RMS of the fluctuations in the streamwise velocity component for the swept wing configuration at y/b=0.55

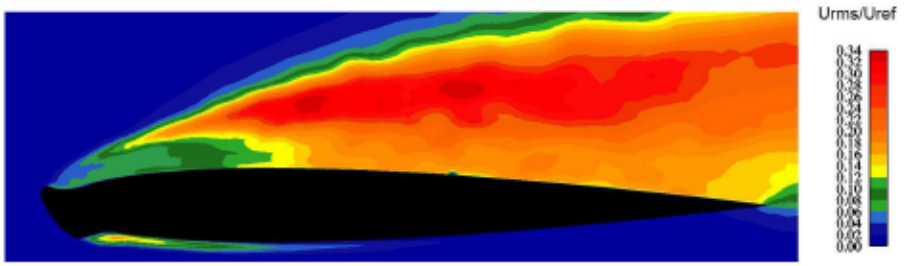

(a) CHEM hybrid RANS/LES

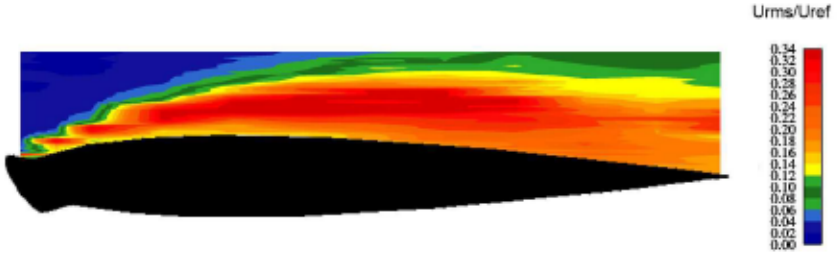

(b) Experimental data [7]

Figure 5.32: Comparison of RMS of the fluctuations in the streamwise velocity component for the swept wing configuration at y/b=0.70

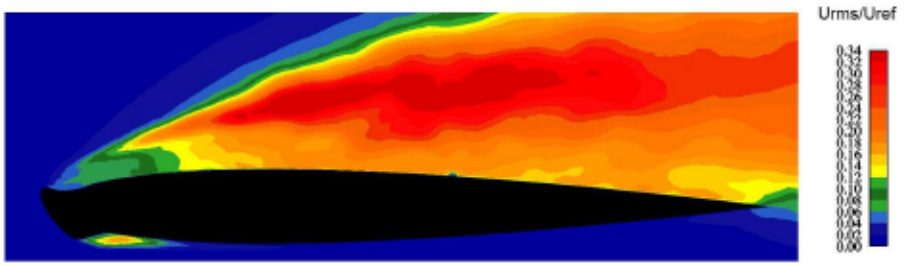

(a) CHEM hybrid RANS/LES

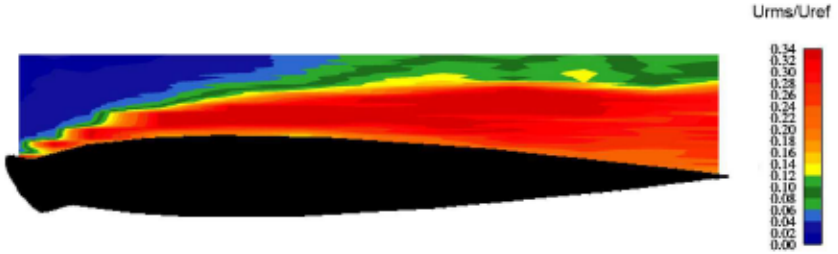

(b) Experimental data [7]

Figure 5.33: Comparison of RMS of the fluctuations in the streamwise velocity component for the swept wing configuration at y/b=0.85

5.3 Summary and Discussion

This section presents a summary of the results presented in the previous section. Additionally, an emphasis is made on placing these results in perspective and understanding their implications.

5.3.1 Summary of Extruded Wing Results

CHEM RANS results for both the 4° and 6° angle of attack cases showed that the extent of the separated region was underpredicted when compared to experimental data. AVUS RANS results, although in good agreement at 4° in terms of the extent of the separated region, significantly overpredict the extent of the separated region at 6° when compared to experimental data. For both the 4° and 6° cases, CHEM RANS results and AVUS RANS results show that the upper surface pressure distributions do not compare favorably with experimental data. In both instances, the recompression region is shifted closer to the leading edge. The lower surface pressure distributions predicted by CHEM RANS are in better agreement with experimental data than those predicted by AVUS. The lift and drag coefficients are underpredicted by the RANS computations of CHEM and AVUS at 4° and 6° angles of attack.

CHEM hybrid RANS/LES results and AVUS DES results show that at 4° angle of attack, the extent of the separated region is slightly overpredicted, whereas at 6°, both CHEM and AVUS significantly overpredict the extent of the separated region. Although the lift coefficients predicted by both AVUS and CHEM are in agreement with experimental results, the drag coefficients are significantly underpredicted. The upper surface pressure distributions predicted by CHEM hybrid RANS/LES and AVUS DES do not compare favorably with experimental data at 4° and 6°

angle of attack. In both cases, the plateau pressure is too high, which may be attributed to the fully turbulent assumption employed for the simulation. The lower surface pressure distributions predicted by CHEM show better agreement with experimental data than do the AVUS results. This may be attributed to the di erence in turbulence models or the use of preconditioning in CHEM. CHEM hybrid RANS/LES results and AVUS DES results show that, although the RMS of the fluctuations in the streamwise velocity is qualitatively similar to the experimental data at 4° and 6° angles of attack, the region where the RMS of the fluctuations in the streamwise velocity is maximum is shifted downstream. Relatively higher intensities of the RMS values were predicted by CHEM in the region near the ice shape when compared to AVUS results. Comparisons of the time-averaged vertical velocity magnitude predicted by CHEM and AVUS with experimental data, in conjunction with the comparisons of the RMS of the fluctuations in the streamwise velocity, show that the qualitative agreement in the the RMS of the fluctuations in the streamwise velocity with experimental data may be partially attributed to shear layer "flapping" rather than due to a shear layer "roll up".

It is seen that, in general, the results predicted by CHEM hybrid RANS/LES solutions and AVUS DES solutions are qualitatively similar when compared to experimental data and both o er improvements over RANS results. It should also be noted that, in general, the CHEM hybrid RANS/LES results and AVUS DES results are in better agreement with the experimental data at 4° angle of attack than at 6° angle of attack, which is nearer to the stall angle.

5.3.2 Summary of Swept Wing Configuration Results

CHEM RANS results exhibited discrepancies in the extent of the separated region when compared to the experimental data at all spanwise locations. The pressure distribution showed a relatively constant pressure region on the upper surface till x/c=0.04 across all spanwise locations after which the pressure increased steadily until reaching the trailing edge. A broader wake was observed at all spanwise locations when compared to corresponding experimental data. The high velocity regions and the high-magnitude reversed flow regions seen in the experimental data was not predicted by CHEM RANS simulation.

Significant di erences were observed in the hybrid RANS/LES results when compared to the RANS results in terms of the pressure distribution and the extent of the separated flow region. CHEM hybrid RANS/LES results showed discrepancies in terms of the extent of the separated flow region and the RMS of the fluctuations in the streamwise velocities when compared to experimental data. Comparison of the RMS of the fluctuations in the streamwise velocities showed the region of maximum fluctuation shifted aft of the experimental data. This shift is similar to that seen in the comparison of the RMS of the fluctuations in the streamwise velocities for the extruded wing configuration.

5.3.3 Discussion

Comparisons of the RMS of the streamwise velocity fluctuations for both the extruded wing and swept wing configurations show that, while the peak magnitudes of the predicted fluctuations are similar to the peaks in the experimental data, the locations of the peaks are shifted downstream. This suggests that the phenomena observed in the experiments are being reproduced in the simulations with a spatial

delay. Taken along with the di erences in the time-averaged vertical velocity magnitude, these results suggest that the simulations predicted the "flapping" of the shear layer but not its "rolling up".

The discrepancies between the experimental data and the hybrid RANS/LES results for the extruded wing and swept wing configuration and the AVUS DES results (for the extruded wing case alone), may be partially attributed to the spatial and temporal accuracy of the flow solvers. Although both CHEM and AVUS computations are formally second-order accurate, the dissipation inherent to the flow solvers may have artificially damped the physical instability. Other research suggests that higher-order solvers, even with their slow rate of convergence for unstructured meshes, may be needed to solve these kinds of problems accurately [60, 61]. If only second-order solvers are available, the use of a relatively coarse mesh contributes to the undesirable dissipation. Although finer mesh spacings in the region containing the detached shear layer may decrease the overall dissipation, it should be noted that the extruded wing mesh used in this e ort has 2.3 million nodes and the swept wing configuration has 4.4 million nodes, and further mesh refinement will lead to very expensive computations. Another contributing factor may also be the use of RANS in the boundary layer which, regardless of solver accuracy, damps out turbulent fluctuations in the attached boundary layer on the ice shape. Thus fluctuations are not present in the detached shear layer causing it to be more stable than it should be.

Comparing the DES and hybrid RANS/LES results for the extruded wing problem, it is seen that, in general, the hybrid RANS/LES results predicted by CHEM are similar to the DES results computed using AVUS. Although there are marked di erences in the RMS of the mean streamwise velocities at midplane, there are only slight di erences between the force coefficients, the extent of the separation

bubble, and the flow reattachment locations. There are some differences in the lower surface pressure distributions and the mean velocity fields that suggest a more extensive separation in the AVUS results than in the CHEM results. Additionally, the predicted mean velocity fields on the lower surface support this conclusion. This demonstrates that the use of preconditioning and a different turbulence model does improve the results obtained, if only on the lower surface.

CHAPTER VI

CONCLUSIONS

6.1 Summary

Computational investigations were carried out to evaluate the e ectiveness and usability of hybrid RANS/LES techniques for predicting unsteady separated flow over wings with ice accretion. Computational work done by Mogili [20] and Mogili *et al.* [21] on an extruded wing with GLC 305/944-ice shape with a rectangular planform using the Spalart-Allmaras DES technique provides the motivation for this current e ort. Two wing models with ice accretion were considered as part of the study: an extruded wing with a two-dimensional 944-glaze-ice shape on a GLC 305 airfoil [5] and a swept wing configuration which consists of a NACA 0012 airfoil section with a simulated glaze-ice accretion with a sweep of 30° [4]. RANS and hybrid RANS/LES computations were performed on the ice wing configurations using the viscous flow solver CHEM [23, 24] using the SST turbulence model and the results were compared with experimental data and the DES results of AVUS. The e ect of preconditioning and the use of a di erent turbulence model was also evaluated by comparing the CHEM results from the extruded wing configuration with corresponding AVUS results.

6.2 Thesis Statement Justification

Hybrid RANS/LES results obtained using CHEM indicate that the e ort to determine whether factors such as the use of preconditioning, a di erent turbulence model or a di erent geometry produces better results has been partially successful. It can be seen that for a hybrid RANS/LES treatment, factors such as the use of preconditioning and a di erent turbulence model slightly a ects the results obtained. The e ect of geometry remains unclear at present. Results also indicate that the use of a higher-order scheme in the hybrid RANS/LES simulations may be necessary in order to obtain acceptable accuracy. Dissipation in the detached shear layer may be reduced by using a finer mesh, but this may be very expensive computationally. Hybrid RANS/LES simulations using CHEM and DES simulations using AVUS show that, in general, the simulations exhibit a less active "roll up" in the detached shear layer when compared to experimental data. The use of RANS in the boundary layer may also contribute to this phenomenon by damping out turbulent fluctuations in the boundary layer on the ice shape.

6.3 Future Work

It is desirable to evaluate the efficacy of higher-order schemes for computing such separated flows. The impact of further mesh refinement, especially in the detached shear layer region, needs to be investigated. There is also a need to closely investigate the causes leading to a relatively stable shear layer to obtain more accurate simulations.

REFERENCES

[1] Potapczuk, M. and Reinmann, J., "Icing Simulation: A Survey of Computer Models and Experimental Facilities," *AGARD CP-496*, 1991, pp. 5.1–5.27.

[2] http://www.aopa.org/.

[3] Gurbacki, H. M. and Bragg, M. B., "Unsteady Aerodynamic Measurements on an Iced Airfoil," 2002, AIAA Paper 2002-0241.

[4] Addy, H., "Ice Accretions and Icing E ects for Modern Airfoils," Tech. Rep. NASA TP-2000-210031, NASA, April 2000.

[5] Addy, H., Zoeckler, J., and Broeren, A., "A Wind Tunnel Study of Icing E ects on a Business Jet Airfoil," 2003, AIAA Paper 2003-0727.

[6] Broeren, A., Addy, H. E., and Bragg, M. B., "Flowfield Measurements about an Airfoil with Leading-Edge Ice Shapes," 2004, AIAA Paper 2004-0559.

[7] Bragg, M. B., M.F.Kerho, and Khodadoust, A., "LDV Flowfield Measurements on a Straight and Swept Wing With a Simulated Ice Accretion," January 1993, AIAA Paper 93-0300, 31st Aerospace Sciences Meeting and Exhibit.

[8] http://www.caa.govt.nz/.

[9] http://www.auf.asn.au/.

[10] Bragg, M. B., Broeren, A. P., and Blumenthal, L. A., "Iced-Airfoil and Wing Aerodynamics," *SAE*, June 2003.

[11] Pan, J. and Loth, E., "Detached Eddy Simulations for Airfoil with Ice Shapes," 2004, AIAA Paper 2004-0564.

[12] Wilcox, D. C., *Turbulence Modeling for CFD*, DCW Industries, Inc., California, 2nd ed., 1998.

[13] Spalart, P. R., Jou, W. H., Strelets, M., and Allmaras, S. R., "Comments on the Feasibility of LES for Wings, and on a Hybrid RANS/LES Approach," *Advances in DNS/LES, 1st AFOSR International Conference on DNS/LES*, August 1997.

[14] Nichols, R. and Nelson, C., "Application of hybrid RANS/LES turbulence models," January 2003, AIAA Paper 20030083, 41st Aerospace Sciences Meeting and Exhibit.

[15] Basu, D., Hamed, A., and Das, K., "DES and Hybrid RANS/LES models for unsteady separated turbulent flow predictions," January 2005, 43rd Aerospace Sciences Meeting and Exhibit.

[16] Kumar, S. and Loth, E., "Detached Eddy Simulations of an Iced-Airfoil," 2001, AIAA Paper 2001-0678.

[17] Kumar, S. and Loth, E., "Aerodynamic Simulations of Airfoils with Upper-Surface Ice-Shapes," *Journal of Aircraft*, Vol. 38, No. 2, March 2001, pp. 285–295.

[18] Shur, M., Spalart, P. R., Strelets, M., and Travin, A., "Detached-Eddy Simulation of an Airfoil at High Angle of Attack," *4th International*

Symposium on Engineering Turbulence Modelling and Experiments, Ajaccio, Corsica, France, May 1999.

[19] Pan, J. and Loth, E., "Reynolds-Averaged NavierStokes Simulations of Airfoils and Wings with Ice Shapes," *Journal of Aircraft*, Vol. 41, No. 4, July-August 2004, pp. 879–891.

[20] Mogili, P., *RANS and DES computations for a three-dimensional wing with ice accretion*, Master's thesis, Mississippi State University, 2004.

[21] Thompson, D., Mogili, P., Chalasani, S., Addy, H., and Choo, Y., "A Computational Icing E ects Study for a Three-Dimensional Wing: Comparison with Experimental Data and Investigation of Spanwise Variation," 2004, AIAA Paper 2004-056.

[22] Tomaro, R. F., Strang, W. Z., and Sankar, L. N., "An Implicit Algorithm for Solving Time Dependent Flows on Unstructured Meshes," 1997, AIAA Paper 1997-0333.

[23] Luke, E., Tang, L., Tong, X., Wu, J., and Cinnella, P., "A Step Towards Shape-Shifting Algorithms: Reactive Flow Simulations Using Generalized Grids," 2001, AIAA Paper 97-0174.

[24] Luke, E., Tong, X., Wu, J., and Cinnella, P., "CHEM 2: A Finite-Rate Viscous Chemistry SolverThe User Guide," Tech. Rep. TR MSSU-COE-ERC-04-07, Mississippi State University, September 2004.

[25] Menter, F., "Zonal Two Equation k-omega Turbulence Models for Aerodynamic Flows," 1993, AIAA Paper 93-2906.

[26] Bragg, M. B., "Rime Ice Accretion and Its E ect on Airfoil Perfomance," *Ph.D Dissertation,Ohio State University and NASA CR 165599*, 1982.

[27] Bragg, M. B. and W.J.Coirier, "Detailed Measurements of the Flow Field in the Vicinity of and Airfoil With Simulated Glaze Ice," January 1986, AIAA Paper 86-04846.

[28] Khodadoust, A. and Bragg, M. B., "Aerodynamics of a Finite Wing with Simulated Ice," *Journal of Aircraft*, Vol. 32, No. 1, 1995.

[29] M.F.Kerho and Bragg, M. B., "Airfoil Boundary-Layer Development and Transition with Large Leading-Edge Roughness," *AIAA Journal*, Vol. 35, No. 1, 1997, pp. 75–84.

[30] Jr., H. A., Miller, D., and R.F.Ide, "A Study of Large Droplet Ice Accretions in the NASA-Lewis IRT at Near-Freezing Conditions:Part 2," 1996, Prepared for the International Conference on Aircraft Inflight Icing,FAA,Springfield,VA.

[31] Lee, S., Dunn, T., Gurbacki, H., Bragg, M., and Loth, E., "An Experimental and Computational Investigation of Spanwise-Step-Ice Shapes on Airfoil Aerodynamics," 1998, AIAA Paper 1998-0490.

[32] Lee, S. and Bragg, M. B., "E ects of Simulated-Spanwise Ice Shapes on Airfoils: Experimental Investigation," 1999, AIAA Paper 1999-0092.

[33] Papadakis, M., Alansatan, S., and Seltmann, M., "Experimental Study of Simulated Ice Shapes On a NACA 0011 Airfoil," 1999, AIAA Paper 1999-0096.

[34] Addy, H., Potapczuk, M., and Sheldon, D., "Modern Airfoil Ice Accretions," January 1997, AIAA Paper 97-0174.

[35] Potapczuk, M. and Gerhart, P., "Progress in the Development of a Naview-Stokes Solver for Evaluation of Iced Airfoil Perfomance," January 1985, AIAA Paper 85-0410.

[36] T.Cebeci, "E ects of Environmentally Imposed Roughness on Airfoil Perfomance," Tech. Rep. NASA CR 179639, NASA, June 1987.

[37] Kwon, O. and Sankar, L., "Numerical Study of the E ects of Icing on Finite Wing Aerodynamics," 1990, AIAA Paper 90-0757.

[38] Potapczuk, M., Bragg, M., Kwon, O., and Sankar, L., "Simulation of Iced Wing Aerodynamics," Tech. Rep. NASA TM-1991-104362, NASA, January 1999.

[39] Dunn, T. A., Loth, E., and Bragg, M. B., "Computational Investigation of Simulated Large-Droplet Ice Shapes on Airfoil Aerodynamics," *Journal of Aircraft*, Vol. 36, No. 5, September 1999, pp. 836–843.

[40] Chung, J., Choo, Y., Reehorst, A., Potapczuk, M., and Slater, J., "Navier-Stokes Analysis of the Flowfield Characteristics of an Ice Contaminated Aircraft Wing," 1999, AIAA Paper 1999-0375.

[41] Chung, J. and Addy, H., "A Numerical Evaluation of Icing E ects on a Natural Laminar Flow Airfoil," 2000, AIAA Paper 2000-0096.

[42] Spalart, P. R. and Allmaras, S. R., "A One-Equation Turbulence Model for Aerodynamic Flows," *La Recherche Aerospatiale*, Vol. 1, 1994, pp. 5–21.

[43] Dunn, T. A. and Loth, E., "E ects of Simulated-Spanwise-Ice Shapes on Airfoils: Computational Investigation," 1999, AIAA Paper 1999-0093.

[44] Luke, E. and George, T., "Loci: A Rule-Based Framework for Parallel Multidisciplinary Simulation Synthesis," *Journal of Functional Programming, Special Issue on Functional Approaches to High-Performance Parallel Programming*, Vol. 15, No. 3, 2005, pp. 477–502, Cambridge University Press.

[45] Venkatakrishnan, V., "On the accuracy of limiters and convergence to steady state solutions," AIAA Paper 93–0880, Jan. 1993.

[46] http://instruct1.cit.cornell.edu/.

[47] http://www.cfd online.com/wiki/.

[48] Luke, E. A., *A rule-base specification system for computational fluid dynamics*, Ph.D. thesis, Mississippi State University, Sept. 1999.

[49] Luke, E., Tong, X., and Cinnella, P., "Numerical Simulations of Fluids with a General Equation of State," January 2006, 44th Aerospace Sciences Meeting and Exhibit.

[50] Bragg, M. B. and M.F.Kerho, "3-D LDV Flowfield Measurements 30-Degree Swept Wing With a Simulated Ice Accretion," Tech. Rep. NASA Contractor Report 195327, University of Illinois at Urbana-Champaign, April 1994.

[51] Spalart, P. R., "Young-Persons Guide to Detached-Eddy Simulation Grids," Tech. Rep. NASA CR-2001-211032, NASA, July 2001.

[52] Choo, Y., Lee, K. D., Thompson, D. S., and Vickerman, M., "Geometry Modeling and Grid Generation for Icing E ects and Ice Accretion Simulations on Airfoils," *Proceedings of the 7th International Conference on Numerical Grid Generation in Computational Field Simulations*, 2000, pp. 1061–1070.

[53] Pirzadeh, S., "Three-Dimensional Unstructured Viscous Grids by the Advancing Layers Method," *AIAA Journal*, Vol. 34, No. 1, January 1996, pp. 43–49.

[54] Samareh, J., "GridTool: A Surface Modeling and Grid Generation Tool, Proceedings of the Workshop on Surface Modeling, Grid Generation, and Related Issues in CFD Solutions," Tech. Rep. NASA CP-3291, NASA, May 1995.

[55] Strang, W. Z., *$Cobalt_{60}$: User's Manual*, September 2000.

[56] http://www.solidworks.com/.

[57] Marcum, D., *Handbook of Grid Generation, J. F. Thompson, B. K. Soni, and N. Weatherill, eds*, chap. Unstructured Grid Generation using Automatic Point Insertion and Local Reconnection, CRC Press, Boca Raton, FL, 2nd ed., 1998.

[58] http://www.hpc.msstate.edu/.

[59] Zaman, K. and Potapczuk, M., *The Low-Frequency Oscillation in the Flow over a NACA 0012 Airfoil with an 'iced' Leading Edge*, New York, 1989, Springer-Verlag.

[60] Darmofal, D. and Fidkowski, K., "Development of a Higher-Order Solver for Aerodynamic Applications," January 2004, 42nd Aerospace Sciences Meeting and Exhibit.

[61] Nastase, C. and Mavriplis, D., "High-Order Discontinuous Galerkin Methods using a Spectral Multigrid Approach," January 2005, 43rd Aerospace Sciences Meeting and Exhibit.